ANL-AFCI-095

Fuel Cycle Methods: First –Order Spherical Harmonics Formulations Capable of Treating Low Density Regions

M. A. Smith, G. Palmiotti
Nuclear Engineering Division
Argonne National Laboratory
9700 South Cass Avenue
Argonne, Illinois 60439

E. E. Lewis
Northwestern University
Department of Mechanical Engineering
Evanston, Illinois 60208

Argonne National Laboratory
9700 S. Cass Avenue
Argonne, IL, 60439, USA

September 2003

Fuel Cycle Methods: First –Order Spherical Harmonics Formulations Capable of Treating Low Density Regions

M. A. Smith, G. Palmiotti
Nuclear Engineering Division
Argonne National Laboratory
9700 South Cass Avenue
Argonne, Illinois 60439

E. E. Lewis
Northwestern University
Department of Mechanical Engineering
Evanston, Illinois 60208

Abstract

In this report we present an approach to deal with a problem encountered in different type of systems and specific configurations: the treatment of low density regions. This is the case of gas cooled reactors, voided configurations (evaluations of associated reactivity coefficients), beam region of external source driven systems, etc. The approach is to form the nodal response matrix using the first-order form of the transport equation, for then the cross section no longer appears in the denominator, as in the case of the standard formulation of the VARIANT code. Two different formulations are presented: the differential and integral ones. After applications to different difficult benchmark problems, it was concluded that the new formulations can treat low density regions.

Table of content

I Introduction

Deterministic analysis codes are used for fuel cycle assessments. Because of the different type of fuel and materials to be adopted in system studies of the short and long term systems, and Gen IV reactors, codes and methods upgrades are needed to improve the capability of correctly evaluating the related advanced fuel cycle strategies. Lattice codes and associated libraries for thermal and fast reactor as well whole core codes need to be upgraded for the new types of fuel and reflectors to be used for different types of strategies involving, MOX, gas cooled, liquid metal cooled systems, with presence of minor actinides and/or fertile free compositions. In this report we will present an approach to deal with a problem encountered in different types of systems and specific configurations: the treatment of low density regions. This is the case for gas cooled reactors, voided configurations (evaluations of associated reactivity coefficients), beam region of external source driven systems, etc.

The variational principle [1] that is the starting point for the variational nodal method implemented in VARIANT [2] cannot be applied directly to voided nodes because of the cross section appearing in the denominator of the even-parity equation. Problems are also encountered when very low-density media occupy a node. A potential alternative for these situations is to form the nodal response matrix using the first-order form of the transport equation, for then the cross section no longer appears in the denominator.

In Section **II** a weighted residual approach is applied to the first-order form of the transport equation assuming the presence of isotropic scattering as well as a source. In Section **III** the same spatial trial functions used in VARIANT are applied both within the node and along the interfaces to discretize the equation in space. In Section **IV**, spherical harmonics approximations are applied to the angular variables using two different methods, referred to as the differential and integral formulations. In both cases, the result is an approximation for the angular flux within the node in terms of the group source and the neutron distribution incoming across the nodal interfaces. In Section **V**, the incoming angular flux distribution and subsequently the angular flux distribution within the node is expressed in terms of the interface variables used in VARIANT. This is necessary if first and second-order methods are to be used in conjunction with one another. In section **VI,** moments of the angular flux at the node interface are derived and response matrices are determined.

From the theory developed in sections **II** through **VI,** both the differential and integral formulations appear to have the potential to provide response matrices compatible with the VARIANT code. Several of these are presently under investigation. The general approach accepted is to first write prototype code in MATHCAD [3] to examine the properties of the response matrix and apply them to small model problems of limited problem size. The ability to treat vacuum nodes is the primary criterion upon

which success is judged. Only those methods with sufficient promise will then be translated to FORTRAN and integrated in the VARIANT code.

Section **VII** presents the current state of the research which is quite encouraging. Both the differential and integral methods have been implemented as prototypic components of the VARIANT code and used successfully to treat benchmark problems that have void regions. Other methods remain in the analysis and debugging stages, with several alternate avenues still to be explored.

II Weighted Residual Treatment of First-Order Equation

Consider the first order form of the transport equation with total and isotropic scattering cross sections σ and σ_s.

$$\hat{\Omega}\cdot\vec{\nabla}\psi(\vec{r},\hat{\Omega})+\sigma\psi(\vec{r},\hat{\Omega})-\sigma_s\phi(\vec{r})-s(\vec{r})=0, \qquad \vec{r}\in V, \qquad (1)$$

with the boundary condition

$$\psi(\vec{r},\hat{\Omega})-\psi_\lambda(\vec{r},\hat{\Omega})=0, \qquad \vec{r}\in\Gamma,\ \hat{n}\cdot\hat{\Omega}<0 \qquad (2)$$

These equations are multiplied by the weight vector $\mathbf{f}(\vec{r})$ and integrated over the spatial domain to obtain the weighted residuals.•

$$\int dV\,\mathbf{f}\left[\hat{\Omega}\cdot\vec{\nabla}\psi+\sigma\psi-\sigma_s\phi-s\right]-\int_{\hat{\Omega}\hat{n}<0} d\Gamma\hat{\Omega}\cdot\hat{n}\mathbf{f}\left[\psi-\psi_\lambda\right]=0 \qquad (3)$$

Employing the divergence theorem,

$$\int dV\,\mathbf{f}\hat{\Omega}\cdot\vec{\nabla}\psi+\int dV\,\psi\ \hat{\Omega}\cdot\vec{\nabla}\mathbf{f}=\int d\Gamma\ \hat{\Omega}\cdot\hat{n}\mathbf{f}\psi, \qquad (4)$$

Eq. (5) is obtained.

$$-\int dV\ \left[\hat{\Omega}\cdot\vec{\nabla}\mathbf{f}\right]\psi+\int dV\,\mathbf{f}\left[\sigma\psi-\sigma_s\phi-s\right]+\int_{\hat{\Omega}n>0} d\Gamma\hat{\Omega}\cdot\hat{n}\mathbf{f}\psi+\int_{\hat{\Omega}n<0} d\Gamma\hat{\Omega}\cdot\hat{n}\mathbf{f}\psi_\lambda=0 \qquad (5)$$

Before proceeding, the general convex surface G is replaced by a sum of flat surfaces G_g each with and outward normal $\hat{n}_g$. For the rectangular, two-dimensional geometries studied in this work, the surfaces are numbered according to the following

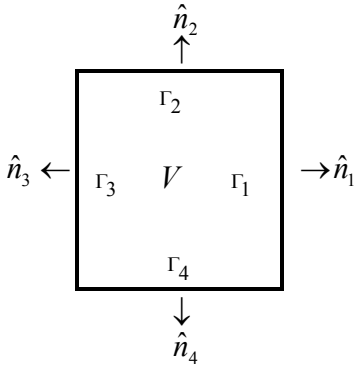

• Bold faced lower and upper case symbols indicate column vectors and matrices, respectively.

III Spatial Discretization

The angular flux is approximated within the domain by

$$\psi(\vec{r},\hat{\Omega}) = \mathbf{f}^T(\vec{r})\boldsymbol{\psi}(\hat{\Omega}), \qquad \vec{r} \in V \quad (6)$$

$$\phi(\vec{r}) = \mathbf{f}^T(\vec{r})\boldsymbol{\psi}_o, \qquad \vec{r} \in V \quad (7)$$

and the boundary condition by

$$\psi_\lambda(\vec{r},\hat{\Omega}) = \mathbf{h}_\gamma^T(\vec{r})\boldsymbol{\psi}_{\lambda\gamma}(\hat{\Omega}), \qquad \vec{r} \in \Gamma_\gamma,\ \hat{n}_\gamma \cdot \hat{\Omega} < 0 \quad (8)$$

where

$$\int_\gamma d\Gamma\, \mathbf{h}_\gamma(\vec{r})\mathbf{h}_\gamma^T(\vec{r}) = \mathbf{I}_\gamma, \quad (9)$$

and

$$\boldsymbol{\psi}_{\lambda\gamma}(\hat{\Omega}) = \int_\gamma d\Gamma \mathbf{h}_\gamma(\vec{r})\psi_\lambda(\vec{r},\hat{\Omega}). \quad (10)$$

Inserting these approximations into Eq. (5) yields

$$\begin{aligned}&\left[-\hat{\Omega}\cdot\int dV(\vec{\nabla}\mathbf{f})\mathbf{f}^T + \int dV\sigma_t\mathbf{f}\mathbf{f}^T + \sum_{\hat{\Omega}\hat{n}_\gamma>0}\hat{\Omega}\cdot\hat{n}_\gamma\int_\gamma d\Gamma\,\mathbf{f}\mathbf{f}^T\right]\boldsymbol{\psi}(\hat{\Omega}) \\ &= \int dV\sigma_s\mathbf{f}\mathbf{f}^T\int d\Omega'\,\boldsymbol{\psi}(\hat{\Omega}') + \mathbf{s} - \sum_{\hat{\Omega}\hat{n}_\gamma<0}\hat{\Omega}\cdot\hat{n}_\gamma\int_\gamma d\Gamma\,\mathbf{f}\,\mathbf{h}_\gamma^T\boldsymbol{\psi}_{\lambda\gamma}(\hat{\Omega})\end{aligned}, \quad (11)$$

and

$$\mathbf{q} = \int dV\mathbf{f}\,q. \quad (12)$$

These equations can be compacted to obtain Eq. (13), by defining the integrals of the spatial trial functions as the matrices in Eqs. (14) through (18).

$$\left[-\sum_k \Omega_k\mathbf{U}_k + \mathbf{F}_t + \sum_{\hat{\Omega}\hat{n}_\gamma>0}\hat{\Omega}\cdot\hat{n}_\gamma\mathbf{W}_\gamma\right]\boldsymbol{\psi}(\hat{\Omega}) = \mathbf{F}_s\int d\Omega'\,\boldsymbol{\psi}(\hat{\Omega}') + \mathbf{s} - \sum_{\hat{\Omega}\hat{n}_\gamma<0}\hat{\Omega}\cdot\hat{n}_\gamma\mathbf{D}_\gamma\boldsymbol{\psi}_{\lambda\gamma}(\hat{\Omega}) \quad (13)$$

$$\mathbf{U}_K = \int dV(\nabla_K\mathbf{f})\mathbf{f}^T \quad (14)$$

$$\mathbf{F} = \int dV\,\mathbf{f}\mathbf{f}^T \quad (15)$$

$$\mathbf{F}_x = \int dV\,\sigma_x\mathbf{f}\mathbf{f}^T \quad (16)$$

$$\mathbf{D}_\gamma = \int d\Gamma_\gamma\mathbf{f}\mathbf{h}_\gamma^T \quad (17)$$

$$\mathbf{W}_\gamma = \int d\Gamma_\gamma\mathbf{f}\mathbf{f}^T \quad (18)$$

IV Angular Approximation- Spherical Harmonics

Next, $\mathbf{y}(\hat{\Omega})$, a vector of spherical harmonics of order *N,* is used to approximate the angular component of the angular flux. The expansion takes the form of

$$\boldsymbol{\psi}(\hat{\Omega}) = \mathbf{y}^T(\hat{\Omega})\otimes\mathbf{I}_s\boldsymbol{\Psi}, \quad (19)$$

where the spherical harmonics obey the orthonormal condition,

$$\int d\Omega\, \mathbf{y}(\hat{\Omega})\mathbf{y}^T(\hat{\Omega}) = \mathbf{I}_\Omega . \tag{20}$$

The identity matrices $\mathbf{I}_s$ and $\mathbf{I}_\Omega$ have the dimensions of **f** and **y**, respectively, and together they form the identity, $\mathbf{I} = \mathbf{I}_s \otimes \mathbf{I}_\Omega$. $\boldsymbol{\Psi}$ is a vector of unknown coefficients for the angular flux expansion. Combining Eqs. (19) and (20) yields the definition in Eq. (21) where the identity in Eq. (22) is used.

$$\boldsymbol{\Psi} = \int d\Omega \Big(\mathbf{y}(\hat{\Omega}) \otimes \mathbf{I}_s\Big)\boldsymbol{\psi}(\hat{\Omega}) \tag{21}$$

$$\begin{aligned}\int d\Omega \Big(\mathbf{y}(\hat{\Omega}) \otimes \mathbf{I}_s\Big)\boldsymbol{\psi}(\hat{\Omega}) &= \int d\Omega \Big(\mathbf{y}(\hat{\Omega}) \otimes \mathbf{I}_s\Big)\Big(\mathbf{y}^T(\hat{\Omega}) \otimes \mathbf{I}_s\Big)\boldsymbol{\Psi} \\ &= \int d\Omega \Big(\mathbf{y}(\hat{\Omega})\mathbf{y}^T(\hat{\Omega}) \otimes \mathbf{I}_s\Big)\boldsymbol{\Psi} \\ &= \boldsymbol{\Psi}\end{aligned} \tag{22}$$

Once $\boldsymbol{\Psi}$ has been determined, the angular flux may be constructed within the node from Eqs (6) and (19).

$$\psi(\vec{r},\hat{\Omega}) = \mathbf{y}^T(\hat{\Omega}) \otimes \mathbf{f}^T(\vec{r})\boldsymbol{\Psi} \tag{23}$$

where the properties of the Kroneker product $\otimes$ are used for the identity in Eq. (24).

$$\begin{aligned}\mathbf{f}^T(\vec{r})\Big(\mathbf{y}^T(\hat{\Omega}) \otimes \mathbf{I}_s\Big) &= \Big[\mathbf{y}(\hat{\Omega}) \otimes \mathbf{I}_s\mathbf{f}(\vec{r})\Big]^T \\ &= \Big[\mathbf{y}(\hat{\Omega}) \otimes \mathbf{f}(\vec{r})\Big]^T \\ &= \mathbf{y}^T(\hat{\Omega}) \otimes \mathbf{f}^T(\vec{r})\end{aligned} \tag{24}$$

Two approaches may be taken to employ spherical harmonics approximations in one of two methods termed the differential and integral methods.

IV.a The Differential Method

To employ the differential method, Eq. (13) is weighted with the vector $\mathbf{I}_s \otimes \mathbf{y}(\hat{\Omega})$ and integrated over angle to obtain Eq. (25).

$$\begin{aligned}&\left[-\sum_k \int d\Omega\, \Omega_k \mathbf{y}\mathbf{y}^T \otimes \mathbf{U}_k + \mathbf{I}_\Omega \otimes \mathbf{F}_t + \sum_\gamma \int_{\hat{\Omega}\cdot\hat{n}_\gamma>0} d\Omega\, \hat{\Omega}\cdot\hat{n}_\gamma \mathbf{y}\mathbf{y}^T \otimes \mathbf{W}_\gamma - \int d\Omega \mathbf{y} \int d\Omega' \mathbf{y}^T \otimes \mathbf{F}_s\right]\boldsymbol{\Psi} \\ &\qquad = \int d\Omega \mathbf{y} \otimes \mathbf{s} - \sum_\gamma \int_{\hat{\Omega}\cdot\hat{n}_\gamma<0} d\Omega\, \hat{\Omega}\cdot\hat{n}_\gamma \mathbf{y} \otimes \mathbf{D}_\gamma \boldsymbol{\psi}_{\lambda\gamma}\end{aligned} \tag{25}$$

Eq. (25) can be simplified to obtain Eq. (26) where the matrices in Eqs. (27) through (30) have been used.

$$\mathbf{A}\boldsymbol{\Psi} = \mathbf{J} \otimes \mathbf{s} - \sum_\gamma \int_{\hat{\Omega}\cdot\hat{n}_\gamma<0} d\Omega\, \hat{\Omega}\cdot\hat{n}_\gamma \mathbf{y}(\hat{\Omega}) \otimes \mathbf{D}_\gamma \boldsymbol{\psi}_{\lambda\gamma}(\hat{\Omega}) \tag{26}$$

$$\mathbf{A} = -\sum_k \mathbf{V}_k \otimes \mathbf{U}_k + \mathbf{I}_\Omega \otimes \mathbf{F}_t + \sum_\gamma \Upsilon_\gamma \otimes \mathbf{W}_\gamma - \mathbf{J}\mathbf{J}^T \otimes \mathbf{F}_s \tag{27}$$

$$\Upsilon_\gamma = \int_{\hat{\Omega}\cdot\hat{n}_\gamma>0} d\Omega\, \hat{\Omega}\cdot\hat{n}_\gamma \mathbf{y}\mathbf{y}^T \tag{28}$$

$$\mathbf{V}_k = \int d\Omega\ \hat{\Omega}_k\ \mathbf{y}\mathbf{y}^T \tag{29}$$

$$\mathbf{J} = \int d\Omega\ \mathbf{y} \tag{30}$$

Inverting **A** and solving for the vector $\boldsymbol{\Psi}$ yields

$$\boldsymbol{\Psi} = \mathbf{A}^{-1}\mathbf{J} \otimes \mathbf{s} - \sum_{\gamma} \mathbf{A}^{-1} \int\limits_{\hat{\Omega}\cdot\hat{n}_\gamma<0} d\Omega\, \hat{\Omega}\cdot\hat{n}_\gamma \mathbf{y}(\hat{\Omega}) \otimes \mathbf{D}_\gamma \boldsymbol{\psi}_{\lambda\gamma}(\hat{\Omega}). \tag{31}$$

Now the angular flux within the node can be reconstructed using Eq. (23).

IV.b The Integral Method.

For the integral form, the spherical harmonics are employed in a different manner. First Eq. (13) is written as a function of angle as done in Eq. (32) with the definition in Eq. (33).

$$\mathbf{A}_\Omega(\hat{\Omega})\boldsymbol{\psi}(\hat{\Omega}) = \mathbf{F}_s\boldsymbol{\psi}_o + \mathbf{s} - \sum_{\hat{\Omega}\cdot\hat{n}_\gamma<0} \hat{\Omega}\cdot\hat{n}_\gamma \mathbf{D}_\gamma \boldsymbol{\psi}_{\lambda\gamma}(\hat{\Omega}) \tag{32}$$

$$\mathbf{A}_\Omega(\hat{\Omega}) = -\sum_k \Omega_k \mathbf{U}_k + \mathbf{F}_t + \sum_{\hat{\Omega}\cdot\hat{n}_\gamma>0} \hat{\Omega}\cdot\hat{n}_\gamma \mathbf{W}_\gamma \tag{33}$$

The scalar flux is given as

$$\boldsymbol{\psi}_o = \int d\Omega\, \boldsymbol{\psi}(\hat{\Omega}). \tag{34}$$

Inverting $\mathbf{A}_\Omega$ and integrating over angle as seen in Eq. (34), the definition of the scalar flux in Eq. (35) is obtained.

$$\boldsymbol{\psi}_o = \int d\Omega\, \mathbf{A}_\Omega^{-1}(\hat{\Omega})\left[\mathbf{F}_s\boldsymbol{\psi}_o + \mathbf{s}\right] - \sum_\gamma \int\limits_{\hat{\Omega}\cdot\hat{n}_\gamma<0} d\Omega\, \hat{\Omega}\cdot\hat{n}_\gamma \mathbf{A}_\Omega^{-1}(\hat{\Omega})\mathbf{D}_\gamma \boldsymbol{\psi}_{\lambda\gamma}(\hat{\Omega}) \tag{35}$$

Solving for the scalar flux, Eq. (36) is obtained with the definition given in Eq. (37).

$$\boldsymbol{\psi}_o = \mathbf{Z}^{-1}\int d\Omega\, \mathbf{A}_\Omega^{-1}(\hat{\Omega})\mathbf{s} - \sum_\gamma \mathbf{Z}^{-1} \int\limits_{\hat{\Omega}\cdot\hat{n}_\gamma<0} d\Omega\, \hat{\Omega}\cdot\hat{n}_\gamma \mathbf{A}_\Omega^{-1}(\hat{\Omega})\mathbf{D}_\gamma \boldsymbol{\psi}_{\lambda\gamma}(\hat{\Omega}) \tag{36}$$

$$\mathbf{Z} = \mathbf{I}_s - \int d\Omega\, \mathbf{A}_\Omega^{-1}(\hat{\Omega})\mathbf{F}_s. \tag{37}$$

Now $\boldsymbol{\psi}_o$ can be eliminated from the right hand side of Eq. (31) and Eq. (38) obtained.

$$\begin{aligned}\mathbf{A}_\Omega(\hat{\Omega})\boldsymbol{\psi}(\hat{\Omega}) = \mathbf{s} + \mathbf{F}_s\mathbf{Z}^{-1}\int d\Omega'\, \mathbf{A}_\Omega^{-1}(\hat{\Omega}')\mathbf{s} - \sum_{\hat{\Omega}\cdot\hat{n}_\gamma<0} \hat{\Omega}\cdot\hat{n}_\gamma \mathbf{D}_\gamma \boldsymbol{\psi}_{\lambda\gamma}(\hat{\Omega}) \\ -\mathbf{F}_s\sum_\gamma \mathbf{Z}^{-1} \int\limits_{\hat{\Omega}\cdot\hat{n}_\gamma<0} d\Omega'\, \hat{\Omega}\cdot\hat{n}_\gamma \mathbf{A}_\Omega^{-1}(\hat{\Omega}')\mathbf{D}_\gamma \boldsymbol{\psi}_{\lambda\gamma}(\hat{\Omega}')\end{aligned} \tag{38}$$

To obtain the angular flux vector $\boldsymbol{\Psi}$ within the domain, $\mathbf{A}_\Omega$ is inverted to obtain $\boldsymbol{\psi}(\hat{\Omega})$. Operating on this equation with $\int d\Omega\, \mathbf{y}(\hat{\Omega}) \otimes \mathbf{I}_s\, \boldsymbol{\Psi}$ yields the angular flux vector within the node domain given by Eq. (39).

$$\boldsymbol{\Psi} = \int d\Omega\, \mathbf{y}(\hat{\Omega}) \otimes \mathbf{A}_{\Omega}^{-1}(\hat{\Omega}) \left[\mathbf{I}_s + \mathbf{F}_s \mathbf{Z}^{-1} \int d\Omega'\, \mathbf{A}_{\Omega}^{-1}(\hat{\Omega}') \right] \mathbf{s}$$
$$- \sum_{\gamma} \int_{\hat{\Omega}\cdot\hat{n}_\gamma<0} d\Omega'\, \hat{\Omega}\cdot\hat{n}_\gamma \left(\mathbf{y}(\hat{\Omega}) \otimes \mathbf{A}_{\Omega}^{-1}(\hat{\Omega}) \mathbf{D}_\gamma \right) \boldsymbol{\psi}_{\lambda\gamma}(\hat{\Omega}) \tag{39}$$
$$- \int d\Omega\, \mathbf{y}(\hat{\Omega}) \otimes \mathbf{A}_{\Omega}^{-1}(\hat{\Omega}) \mathbf{F}_s \mathbf{Z}^{-1} \sum_{\gamma} \int_{\hat{\Omega}\cdot\hat{n}_\gamma<0} d\Omega'\, \hat{\Omega}\cdot\hat{n}_\gamma \mathbf{A}_{\Omega}^{-1}(\hat{\Omega}') \mathbf{D}_\gamma \boldsymbol{\psi}_{\lambda\gamma}(\hat{\Omega}')$$

Eq. (39) can be written more compactly as shown in Eqs. (40) and (41) where the new matrices are defined by Eqs. (42) and (43).

$$\boldsymbol{\Psi} = \mathbf{C} \left[\mathbf{I}_s + \mathbf{F}_s \mathbf{Z}^{-1} \mathbf{C}_0 \right] \mathbf{s}$$
$$- \sum_{\gamma} \int_{\hat{\Omega}\cdot\hat{n}_\gamma<0} d\Omega'\, \hat{\Omega}\cdot\hat{n}_\gamma \mathbf{y}(\hat{\Omega}) \otimes \mathbf{A}_{\Omega}^{-1}(\hat{\Omega}) \mathbf{D}_\gamma \boldsymbol{\psi}_{\lambda\gamma}(\hat{\Omega}) \tag{40}$$
$$- \mathbf{C} \mathbf{F}_s \mathbf{Z}^{-1} \sum_{\gamma} \int_{\hat{\Omega}\cdot\hat{n}_\gamma<0} d\Omega'\, \hat{\Omega}\cdot\hat{n}_\gamma \mathbf{A}_{\Omega}^{-1}(\hat{\Omega}') \mathbf{D}_\gamma \boldsymbol{\psi}_{\lambda\gamma}(\hat{\Omega}')$$

$$\boldsymbol{\Psi} = \mathbf{C} \left[\mathbf{I}_s + \mathbf{F}_s \mathbf{Z}^{-1} \mathbf{C}_0 \right] \mathbf{s} - \sum_{\gamma} \int_{\hat{\Omega}\cdot\hat{n}_\gamma<0} d\Omega\, \hat{\Omega}\cdot\hat{n}_\gamma \left[\mathbf{y}(\hat{\Omega}) \otimes \mathbf{I}_s + \mathbf{C} \mathbf{F}_s \mathbf{Z}^{-1} \right] \mathbf{A}_{\Omega}^{-1}(\hat{\Omega}) \mathbf{D}_\gamma \boldsymbol{\psi}_{\lambda\gamma}(\hat{\Omega}) \tag{41}$$

$$\mathbf{C}_0 = \int d\Omega\, \mathbf{A}_{\Omega}^{-1}(\hat{\Omega}) \tag{42}$$

$$\mathbf{C} = \int d\Omega\, \mathbf{y}(\hat{\Omega}) \otimes \mathbf{A}_{\Omega}^{-1}(\hat{\Omega}) \tag{43}$$

IV.c Combined Notation

Both the differential and integral formulations can be treated together by writing Eqs. (31) and (41) in the form

$$\boldsymbol{\Psi} = \mathbf{q} - \sum_{\gamma} \int_{\hat{\Omega}\cdot\hat{n}_\gamma<0} d\Omega\, \hat{\Omega}\cdot\hat{n}_\gamma \mathbf{H}(\hat{\Omega}) \mathbf{D}_\gamma \boldsymbol{\psi}_{\lambda\gamma}(\hat{\Omega}). \tag{44}$$

For the differential formulation, $\mathbf{q}$ and $\mathbf{H}(\hat{\Omega})$ are given by Eqs. (45) and (46).

$$\mathbf{q} = \mathbf{A}^{-1} \mathbf{J} \otimes \mathbf{s} \tag{45}$$

$$\mathbf{H}(\hat{\Omega}) = \mathbf{A}^{-1} \mathbf{y}(\hat{\Omega}) \otimes \mathbf{I}_s \tag{46}$$

For the integral formulation, $\mathbf{q}$ and $\mathbf{H}(\hat{\Omega})$ are given by Eqs. (47) and (48).

$$\mathbf{q} = \mathbf{C} \left[\mathbf{I}_s + \mathbf{F}_s \mathbf{Z}^{-1} \mathbf{C}_0 \right] \mathbf{s} \tag{47}$$

$$\mathbf{H}(\hat{\Omega}) = \left[\mathbf{y}(\hat{\Omega}) \otimes \mathbf{I}_s + \mathbf{C} \mathbf{F}_s \mathbf{Z}^{-1} \right] \mathbf{A}_{\Omega}^{-1}(\hat{\Omega}) \tag{48}$$

V. Interface Conditions

Next, $\boldsymbol{\psi}_{\lambda\gamma}(\hat{\Omega})$, the vector of spatial moments of the angular flux on the node surface, must be related to the even- and odd-parity space-angle moments employed in VARIANT. In VARIANT, even- and odd-parity spherical harmonics expansions are used to represent the angular flux distribution within the node volume and on its surface,

respectively. These expansions can be combined to express the space-angle distribution of the flux at the nodal surface as

$$\psi(\vec{r},\hat{\Omega}) = \mathbf{y}_+^T(\hat{\Omega}) \otimes \mathbf{f}^T(\vec{r})\boldsymbol{\xi} + \mathbf{y}_-^T(\hat{\Omega})\mathbf{K}_\gamma \Lambda \otimes \mathbf{h}^T(\vec{r})\boldsymbol{\chi}_\gamma . \qquad \vec{r} \in \Gamma_\gamma \quad (49)$$

Here, $\mathbf{f}(\vec{r})$ and $\mathbf{h}(\vec{r})$ are the same vectors of continuous trial functions defined for $\vec{r} \in V$ and $\vec{r} \in \Gamma$, respectively. $\mathbf{y}_+(\hat{\Omega})$ and $\mathbf{y}_-(\hat{\Omega})$ are vectors of the even- and odd-parity spherical harmonics where

$$\mathbf{y}\ (\hat{\Omega}) = \begin{bmatrix} \mathbf{y}_+(\hat{\Omega}) \\ \mathbf{y}_-(\hat{\Omega}) \end{bmatrix}. \quad (50)$$

In VARIANT, the odd parity spherical harmonics are rotated to align the polar angle with the outgoing normal. The square matrix $\mathbf{K}_\gamma$ is defined to represent the rotation from $\hat{n}_\gamma$ to the reference direction $\hat{n}_o$ as shown in Eq. (51).

$$\mathbf{y}_-(\hat{\Omega}) = \mathbf{K}_\gamma \mathbf{y}_{\gamma-}(\hat{\Omega}) \quad (51)$$

$$\mathbf{K}_\gamma = \int d\Omega \mathbf{y}_-(\hat{\Omega})\mathbf{y}_{\gamma-}^T(\hat{\Omega}) \quad (52)$$

Also since $\mathbf{K}_\gamma^T = \mathbf{K}_\gamma^{-1}$, Eq. (51) can be written as

$$\mathbf{y}_{\gamma-}(\hat{\Omega}) = \mathbf{K}_\gamma^T \mathbf{y}_-(\hat{\Omega}) . \quad (53)$$

The $\boldsymbol{\Lambda}$ matrix extracts the necessary linear combinations of the odd-parity flux moments that must be continuous across the interface. In VARIANT, two such sets of angular interface functions, and thus $\boldsymbol{\Lambda}$, have been defined: the LI (linearly independent) set [4] and the Rumyantsev set [5].

The hybrid nodal method, upon which VARIANT is based, requires both $\boldsymbol{\chi}_\gamma$ and $\boldsymbol{\varphi}_\gamma$ to be continuous across nodal interfaces, where $\boldsymbol{\varphi}_\gamma$ is given by Eqs. (54) and (55).

$$\boldsymbol{\varphi}_\gamma = \Lambda^T \mathbf{K}_\gamma^T \mathbf{E}_\gamma^T \otimes \mathbf{D}_\gamma^T \boldsymbol{\xi} \quad (54)$$

$$\mathbf{E}_\gamma = \int d\Omega\, \hat{\Omega} \cdot \hat{n}_\gamma \mathbf{y}_+(\hat{\Omega})\mathbf{y}_-^T(\hat{\Omega}) \quad (55)$$

To express $\boldsymbol{\psi}_{\lambda\gamma}(\hat{\Omega})$, which appears in Eq. (44), in terms of $\boldsymbol{\varphi}_\gamma$ and $\boldsymbol{\chi}_\gamma$, ψ_λ in Eq.(10) is set equal to ψ in Eq. (49) to produce Eq. (56).

$$\boldsymbol{\psi}_{\lambda\gamma}(\hat{\Omega}) = \int_\gamma d\Gamma\, \mathbf{h}_\gamma(\vec{r}) \left[\mathbf{y}_+^T(\hat{\Omega}) \otimes \mathbf{f}^T(\vec{r})\boldsymbol{\xi} + \mathbf{y}_-^T(\hat{\Omega})\mathbf{K}_\gamma \Lambda \otimes \mathbf{h}^T(\vec{r})\boldsymbol{\chi}_\gamma \right] \qquad \hat{n}_\gamma \cdot \hat{\Omega} < 0 \quad (56)$$

Using Eqs. (9) and (17) along with the properties of the $\otimes$ operator, Eq. (56) simplifies to

$$\boldsymbol{\psi}_{\lambda\gamma}(\hat{\Omega}) = \mathbf{y}_+^T(\hat{\Omega})\mathbf{I}_\Omega^+ \otimes \mathbf{D}_\gamma^T \boldsymbol{\xi} + \mathbf{y}_-^T(\hat{\Omega})\mathbf{K}_\gamma \Lambda \otimes \mathbf{I}_\gamma \boldsymbol{\chi}_\gamma , \qquad \hat{n}_\gamma \cdot \hat{\Omega} < 0 \quad (57)$$

where the identity operator $\mathbf{I}_\Omega^+$ has the dimension of $\mathbf{y}_+$. To replace $\boldsymbol{\xi}$ with $\boldsymbol{\varphi}_\gamma$ in Eq. (57), Eq. (54) is multiplied by $(\Lambda^T \mathbf{K}_\gamma^T \mathbf{E}_\gamma^T)^{-1} \otimes \mathbf{I}_\gamma$ to yield the identity relation of Eq. (58).

$$(\Lambda^T\mathbf{K}_\gamma^T\mathbf{E}_\gamma^T)^{-1}\otimes\mathbf{I}_\gamma\boldsymbol{\varphi}_\gamma=\left[(\Lambda^T\mathbf{K}_\gamma^T\mathbf{E}_\gamma^T)^{-1}\otimes\mathbf{I}_\gamma\right]\left[\Lambda^T\mathbf{K}_\gamma^T\mathbf{E}_\gamma^T\otimes\mathbf{D}_\gamma^T\right]\boldsymbol{\xi}$$
$$=\left[(\Lambda^T\mathbf{K}_\gamma^T\mathbf{E}_\gamma^T)^{-1}\Lambda^T\mathbf{K}_\gamma^T\mathbf{E}_\gamma^T\right]\otimes\mathbf{I}_\gamma\mathbf{D}_\gamma^T\boldsymbol{\xi} \qquad (58)$$
$$=\mathbf{I}_\Omega^+\otimes\mathbf{D}_\gamma^T\boldsymbol{\xi}$$

Substituting Eq. (58) into Eq. (57) produces Eq. (59).

$$\boldsymbol{\psi}_{\lambda\gamma}(\hat{\Omega})=\mathbf{y}_+^T(\hat{\Omega})(\Lambda^T\mathbf{K}_\gamma^T\mathbf{E}_\gamma^T)^{-1}\otimes\mathbf{I}_\gamma\boldsymbol{\varphi}_\gamma+\mathbf{y}_-^T(\hat{\Omega})\mathbf{K}_\gamma\Lambda\otimes\mathbf{I}_\gamma\boldsymbol{\chi}_\gamma \qquad \hat{n}_\gamma\cdot\hat{\Omega}<0 \quad (59)$$

Using the properties of $\otimes$ once again, Eq. (59) is simplified to

$$\mathbf{D}_\gamma\boldsymbol{\psi}_{\lambda\gamma}(\hat{\Omega})=\mathbf{y}_+^T(\hat{\Omega})(\Lambda^T\mathbf{K}_\gamma^T\mathbf{E}_\gamma^T)^{-1}\otimes\mathbf{D}_\gamma\boldsymbol{\varphi}_\gamma+\mathbf{y}_-^T(\hat{\Omega})\mathbf{K}_\gamma\Lambda\otimes\mathbf{D}_\gamma\boldsymbol{\chi}_\gamma. \qquad (60)$$

Finally, Eq. (60) is substituted into Eq. (44) resulting in

$$\boldsymbol{\Psi}=\mathbf{q}-\sum_\gamma\int_{\hat{\Omega}\hat{n}_\gamma<0}d\Omega\,\hat{\Omega}\cdot\hat{n}_\gamma\mathbf{H}(\hat{\Omega})\left[\mathbf{y}_+^T(\hat{\Omega})(\Lambda^T\mathbf{K}_\gamma^T\mathbf{E}_\gamma^T)^{-1}\otimes\mathbf{D}_\gamma\boldsymbol{\varphi}_\gamma+\mathbf{y}_-^T(\hat{\Omega})\mathbf{K}_\gamma\Lambda\otimes\mathbf{D}_\gamma\boldsymbol{\chi}_\gamma\right]. \quad (61)$$

Eq. (61) can be expressed as Eq. (62) using the matrix definitions in Eq. (63).

$$\boldsymbol{\Psi}=\mathbf{q}-\sum_\gamma\left[\mathbf{M}_\gamma^+(\Lambda^T\mathbf{K}_\gamma^T\mathbf{E}_\gamma^T)^{-1}\otimes\mathbf{D}_\gamma\boldsymbol{\varphi}_\gamma+\mathbf{M}_\gamma^+\mathbf{K}_\gamma\Lambda\otimes\mathbf{D}_\gamma\boldsymbol{\chi}_\gamma\right] \qquad (62)$$

$$\mathbf{M}_\gamma^\pm=\int_{\hat{\Omega}\hat{n}_\gamma<0}d\Omega\,\hat{\Omega}\cdot\hat{n}_\gamma\mathbf{H}(\hat{\Omega})\mathbf{y}_\pm^T(\hat{\Omega}) \qquad (63)$$

The $\mathbf{M}_\gamma^\pm$ matrices for the differential case are given as

$$\mathbf{M}_\gamma^\pm=\mathbf{A}^{-1}\int_{\hat{\Omega}\hat{n}_\gamma<0}d\Omega\,\hat{\Omega}\cdot\hat{n}_\gamma\mathbf{y}(\hat{\Omega})\otimes\mathbf{I}_s\mathbf{y}_\pm^T(\hat{\Omega}), \qquad (64)$$

while for the integral case they are

$$\mathbf{M}_\gamma^\pm=\int_{\hat{\Omega}\hat{n}_\gamma<0}d\Omega\,\hat{\Omega}\cdot\hat{n}_\gamma\left[\mathbf{y}(\hat{\Omega})\otimes\mathbf{I}_s+\int d\Omega'\,\mathbf{y}(\hat{\Omega}')\otimes\mathbf{A}_\Omega^{-1}(\hat{\Omega}')\mathbf{F}_s\mathbf{Z}^{-1}\right]\mathbf{A}_\Omega^{-1}(\hat{\Omega})\mathbf{y}_\pm^T(\hat{\Omega}). \qquad (65)$$

VI. Response Matrices

At this point an expression has been obtained for the angular flux distribution within the node in terms of the interface conditions for the incoming flux. This was accomplished by substituting $\boldsymbol{\Psi}$, determined from Eq. (62), into Eq. (23). To obtain response matrices, continuity conditions must be imposed on the angular flux across the interfaces. Recall that the boundary condition given by Eq. (59), which specifies the angular distribution of the incoming flux (for $\hat{n}_\gamma\cdot\hat{\Omega}<0$) in terms of $\boldsymbol{\varphi}_\gamma$ and $\boldsymbol{\chi}_\gamma$, is the approximation to Eq. (2). If Eq. (66) is also used, Eq. (67) can be obtained from Eqs. (10), (17), and (23).

$$\psi(\vec{r},\hat{\Omega})-\psi_\lambda(\vec{r},\hat{\Omega})=0 \qquad \vec{r}\in\Gamma,\ \hat{n}\cdot\hat{\Omega}>0 \quad (66)$$

$$\boldsymbol{\psi}_{\lambda\gamma}(\hat{\Omega})=\mathbf{y}^T(\hat{\Omega})\otimes\mathbf{D}_\gamma^T\boldsymbol{\Psi} \qquad \hat{n}_\gamma\cdot\hat{\Omega}>0 \quad (67)$$

The even and odd parity components can be treated separately, thereby obtaining Eqs. (68) and (69) where the Boolean matrices of Eq. (20) and the identity $\boldsymbol{\Lambda}^T\boldsymbol{\Lambda}=\mathbf{I}$ have been used.

$$\boldsymbol{\varphi}_\gamma=\Lambda^T\mathbf{K}_\gamma^T\mathbf{E}_\gamma^T\Xi_+\otimes\mathbf{D}_\gamma^T\boldsymbol{\Psi} \qquad (68)$$

$$\boldsymbol{\chi}_\gamma = \boldsymbol{\Lambda}^T \mathbf{K}_\gamma^T \Xi_- \otimes \mathbf{D}_\gamma^T \boldsymbol{\Psi} \tag{69}$$

$$\Xi_\pm = \int d\Omega \; \mathbf{y}_\pm^T(\hat{\Omega}) \mathbf{y}^T(\hat{\Omega}) \tag{70}$$

Continuity can be imposed on Eq. (68), Eq. (69), or a linear combination of the two. Using weights of $\frac{1}{2}a$ and b, which are free parameters, Eqs. (68) and (69) can be linearly combined as shown in Eqs. (71) and (72).

$$\tfrac{1}{2}a\boldsymbol{\varphi}_\gamma + b\boldsymbol{\chi}_\gamma = \boldsymbol{\Pi}_\gamma \boldsymbol{\Psi} \tag{71}$$

$$\boldsymbol{\Pi}_\gamma = \Lambda^T \mathbf{K}_\gamma^T (\tfrac{1}{2}a \mathbf{E}_\gamma^T \Xi_+ + b\Xi_-) \otimes \mathbf{D}_\gamma^T \tag{72}$$

Combining Eqs. (62) and (71), Eq. (73) is obtained

$$\tfrac{1}{2}a\boldsymbol{\varphi}_\gamma + b\boldsymbol{\chi}_\gamma = \boldsymbol{\Pi}_\gamma \mathbf{q} - \sum_{\gamma'} \boldsymbol{\Pi}_\gamma \mathbf{M}_{\gamma'}^+ (\Lambda^T \mathbf{K}_{\gamma'}^T \mathbf{E}_{\gamma'}^T)^{-1} \otimes \mathbf{D}_{\gamma'} \boldsymbol{\varphi}_{\gamma'} - \sum_{\gamma'} \boldsymbol{\Pi}_\gamma \mathbf{M}_{\gamma'}^- \mathbf{K}_{\gamma'} \Lambda \otimes \mathbf{D}_{\gamma'} \boldsymbol{\chi}_{\gamma'} . \tag{73}$$

The variable transformation implemented in VARIANT can now be implemented here by introducing the partial current variables of Eq. (74).

$$\mathbf{j}_\gamma^\pm = \tfrac{1}{4}\boldsymbol{\varphi}_\gamma \pm \tfrac{1}{2}\boldsymbol{\chi}_\gamma \tag{74}$$

Inserting Eq. (74) into Eq. (73) yields Eq. (75).

$$(a+b)\mathbf{j}_\gamma^+ + (a-b)\mathbf{j}_\gamma^- = \mathbf{s}_\gamma - \sum_{\gamma'} \mathbf{G}_{\gamma\gamma'}^+ \mathbf{j}_{\gamma'}^+ - \sum_{\gamma'} \mathbf{G}_{\gamma\gamma'}^- \mathbf{j}_{\gamma'}^- \tag{75}$$

The source component, $\mathbf{s}_\gamma$, is given by Eq. (76) while the $\mathbf{G}_{\gamma\gamma'}^\pm$ matrices are given by Eq. (77).

$$\mathbf{s}_\gamma = \boldsymbol{\Pi}_\gamma \mathbf{q} \tag{76}$$

$$\mathbf{G}_{\gamma\gamma'}^\pm = 2\boldsymbol{\Pi}_\gamma \mathbf{M}_{\gamma'}^+ (\Lambda^T \mathbf{K}_{\gamma'}^T \mathbf{E}_{\gamma'}^T)^{-1} \otimes \mathbf{D}_{\gamma'} \pm \boldsymbol{\Pi}_\gamma \mathbf{M}_{\gamma'}^- \mathbf{K}_{\gamma'} \Lambda \otimes \mathbf{D}_{\gamma'} . \tag{77}$$

Equation (75) can be partitioned with respect to the nodal interfaces to produce Eq. (78).

$$(a+b)\mathbf{j}^+ + (a-b)\mathbf{j}^- = \mathbf{s} \; - \mathbf{G}^+ \mathbf{j}^+ - \mathbf{G}^- \mathbf{j}^- . \tag{78}$$

Solving for $\mathbf{j}^+$, the familiar response matrix equation given by Eq. (79) results, where the new matrices are defined in Eqs. (80) and (81).

$$\mathbf{j}^+ = \mathbf{R}\,\mathbf{j}^- + \mathbf{B}\,\mathbf{s} \tag{79}$$

$$\mathbf{R} = \left[(a+b)\mathbf{I} + \mathbf{G}^+ \right]^{-1} \left[(b-a)\mathbf{I} - \mathbf{G}^- \right] \tag{80}$$

$$\mathbf{B} = \left[(a+b)\mathbf{I} + \mathbf{G}^+ \right]^{-1} \tag{81}$$

As mentioned earlier, the above matrix relationships have been implemented in MATHCAD and tested for stability and accuracy. In all of these tests, both formulations conserved neutrons and performed well. To more thoroughly investigate the methods, translation to FORTRAN is required, and thus both formulations were made compatible with the VARIANT code. What follows in Section **VII** is a brief discussion of the numerical results obtained for several fundamental benchmarks using the FORTRAN translations.

VII. Results

The response matrix formulation for the differential formulation has only been implemented in MATHCAD. Since the outer iteration solver in MATHCAD can only

solve problems of limited size (~50 nodes), a patch was made for the VARIANT coding such that the outer iterations could be performed in VARIANT using the MATHCAD response matrices for larger problems. This reduced the overall coding time that would have been necessary to investigate the first order formulations. Also, the angular matrices of Eqs. (28) through (30) are difficult to implement in the existing VARIANT coding while in MATHCAD they are quite trivial. The solutions obtained using the modified VARIANT coding for the first order differential method is referred to as VARIANT-F.

The response matrix formulation for the first order integral method has been implemented in MATHCAD and into a prototypic version of the VARIANT code. The MATHCAD coding is extremely limited due to the angular integrations in Eq. (65). The implementation into VARIANT was only possible due to the existence of the FORTRAN coding for the second order integral method of previous work [6]. However, the response matrix formalism given above for the first order integral method required Eq. (65) to be rewritten in an even-parity form to allow it to be compatible with the existing coding in VARIANT. As a consequence, only one interface condition was possible for the free parameters a and b (a=2, b=0). The impact of the altered response matrix formulation and the use of alternate interface conditions upon the accuracy and stability of the first order integral method is unknown at this time. The solutions obtained using the first order integral form implemented into VARIANT will be referred to as VARIANT-FI.

Three two-dimensional, fixed source benchmark problems were chosen to test the new formulations. In all three benchmarks, the average flux within each node (mesh) is used to assess the accuracy of the method rather than relying upon a rigorous reconstruction of the flux. The first benchmark is by Azmy[7], the geometry for which is given in Figure 1. As can be seen, the AZMY benchmark is a deep penetration problem that can be solved well using the VARIANT code (even-parity, second order differential formulation) or a collision probability code such as DRAGON [8]. However, because of the large number of meshes chosen for use in the flux solution, a precise collision probably solution utilizing a very refined space-angle approximation, was not possible and thus the VARIANT P_{21} solution was taken as the reference. This benchmark will display any general problems with the first order differential or integral methods investigated in this work.

The second and third benchmarks are modifications of a Watanabe-Maynard benchmark[8-9], the geometry for which is given in Figure 2. The original benchmark used the problem 1 (P1) cross sections in Figure 2 with a larger source region and smaller source magnitude. The benchmark dimensions were simplified for this work to reduce the computational burden for MATHCAD. The problem 2 (P2) cross sections were introduced to make the problem similar to that of the AZMY benchmark and thus more difficult. Both of these benchmarks can be used as extremes to assess the accuracy of the void treatment for the first order differential and integral formulations. The reference solution was obtained using the DRAGON code since VARIANT cannot solve this problem. Consequently, a relatively coarse mesh had to be used for the flux solution. For all three benchmark problems, the same spatial approximation is implemented in the

VARIANT and VARIANT-FI coding. For additional perspective, discrete ordinate solutions for all three benchmark problems are provided using TWODANT [10].

VII.a AZMY Benchmark

No theoretical justification has yet been established which would indicate optimum values for the free parameters *a* and *b*. As a result, for the differential form, four different values of the free parameters *a* and *b* were considered, which are given in Table I. These values were chosen because they had the obvious physical interpretations also listed in Table I. From the boundary condition given by Eq. (66) and implemented in Eq. (71), these interface conditions are referred to as bounded $\boldsymbol{\varphi}_\gamma$, bounded $\boldsymbol{\chi}_\gamma$, bounded $\mathbf{j}^+$, and bounded $\mathbf{j}^-$ in accordance with Table I. From numerical studies, the bounded $\mathbf{j}^-$ condition has been eliminated because it results in a singular response matrix and thus cannot produce a solvable system of equations.

Figure 3 gives the VARIANT and DRAGON flux traverse along the vacuum boundary indicated by the line in Figure 2. Also included is a TWODANT solution which is comparable with the solutions given by VARIANT and VARIANT-F. As can be seen, it is difficult to distinguish the VARIANT P_{11}, VARIANT P_{21}, and DRAGON solutions on the graph. A maximum 5% error was found to exist between the DRAGON and VARIANT P_{21} solution, which was found to be caused by an inadequate mesh refinement in the DRAGON solution.

Figures 4, 5, and 6, respectively give the VARIANT-F bounded $\boldsymbol{\varphi}_\gamma$, bounded $\boldsymbol{\chi}_\gamma$, and bounded $\mathbf{j}^+$ solutions for the AZMY benchmark using the LI interface angular trial function set [4]. Figures 7, 8, and 9, give the VARIANT-F bounded $\boldsymbol{\varphi}_\gamma$, bounded $\boldsymbol{\chi}_\gamma$, and bounded $\mathbf{j}^+$ solutions for the AZMY benchmark using the Rumyantsev interface angular trial function set [5]. Of all of the first order differential solutions, the bounded $\boldsymbol{\varphi}_\gamma$ interface condition produces solutions that could be interpreted as "closest" to the reference solution. However, for the LI set at P_9, the maximum error is 35% and the average error is 23%, while for the Rumyantsev set the maximum error is 11% and the average error is 6%. By comparison, for the second order differential method employed in VARIANT (see Figure 3) the maximum error for the P_9 approximation is 3% and the average error is 0.37%.

The bounded $\boldsymbol{\chi}_\gamma$ interface condition generally yields the worst solutions, and contains errors far greater than 200%. The bounded $\mathbf{j}^+$ interface condition appears to simply be a combination of the accuracies of the bounded $\boldsymbol{\varphi}_\gamma$ condition with the inaccuracies of the bounded $\boldsymbol{\chi}_\gamma$ condition. This behavior is believed to be caused by the use of odd P_N boundary conditions that are based on the second order even-parity

formulation. For the second order even-parity formulation, bounded φ_γ is the only appropriate choice. If even P_N boundary conditions were imposed (those for a second order odd-parity formulation) then it is reasonable to assume that the bounded χ_γ condition would produce more accurate solutions.

The unresolved discrepancies in the first order differential method are believed to be caused by an insufficient space-angle approximation. However, because of the expense of the first order differential method, no further work was carried out to prove this, especially when considering that an angular approximation far greater than P_9 would be necessary to reach full angular convergence. The different behavior of the LI and Rumyantsev interface angular sets is also unexplained. From previous experience with VARIANT, the two expansion sets have produced indistinguishable solutions at every P_N level (~0.000% error) for every problem. In general, the results of the first order differential method are unsatisfactory because they indicate that more space-angle refinement is necessary to obtain a solution in the first order differential method than that of the second order differential method.

Unlike the first order differential solutions given above, Figure 10 gives the VARIANT-FI solutions (only the Rumyantsev angular trial function set is valid for the integral method). For additional comparison, results for the even-parity, second order integral method (VARIANT-I) have also been included. From Figure 10, as the P_N order is refined, the VARIANT-FI results rapidly approach the reference solution. However, similar to the first order differential method, when the VARIANT-FI results are compared to the VARIANT-I results, the latter converge faster. For the VARIANT-I coding, the P_4 result is difficult to distinguish from the reference solution and therefore was not included. In contrast, the P_4 VARIANT-FI solution has substantially more error than VARIANT-I. At P_{12} there are still are also some visible discrepancies that still exist between the VARIANT-FI and the VARIANT reference solution so a closer inspection of the flux accuracy is provided.

Figure 11 gives the magnitude of the calculated error (absolute value) for the P_{12} and P_{22}, VARIANT-I and VARIANT-FI solutions along with the error for the P_{11} VARIANT solution. For P_{12} solutions the error in the VARIANT-FI solution is clearly larger than that of the VARIANT-I result. At P_{22}, which is approaching the point of angular convergence, the VARIANT-I and VARIANT-FI solutions have roughly the same amount of error all of which is substantially less than 1%. In general, the errors in the VARIANT-FI and VARIANT-I flux solutions are small, but clearly the VARIANT-I coding obtains a much more accurate solution with less effort. For perspective it is important to note that the VARIANT-I and VARIANT-FI solutions are more accurate than the TWODANT solutions for the same angular order.

VII.b Modified Watanabe-Maynard Problem 1

In the AZMY benchmark, no apparent problems were found with either the response matrix formulation or the red-black outer iteration solution procedure for the first order differential form. The first order differential method simply produced solutions that were not as accurate as the second order differential form. The first order differential method was implemented on the Watanabe-Maynard benchmarks to see if further degradation of the solution would occur. Given the inaccuracy for the AZMY benchmark, it is to no surprise that the bounded χ_γ and bounded $\mathbf{j}^+$ interface conditions both failed to produce meaningful solutions. Unexpectedly, the LI set was eliminated because it tended to diverge rather than converge during the outer iterations. As a consequence, only solutions for the bounded φ_γ interface condition using the Rumyantsev interface angular set are available.

In this benchmark, the four flux traverses shown on the right hand side of Figure 2 are investigated. Figures 12, 13, 14, and 15 give the four flux traverse solutions for the first order differential solutions. As can be seen, three solutions are given for the P_9 approximation in each figure with the numbers in parenthesis indicating the total number of iterations used in the problem solution. The reason for their inclusion is a consequence of the fact that none of the solutions succeeded in reaching the specified convergence (1E-6). However, what is clear from Figures 12 through 15 is that the VARIANT-F solutions are converging, but they effectively require an infinite number of iterations. The reason for the convergence problems is at present unknown, but acceleration may be able to overcome the problems.

From Figures 12 through 15, it is clear that a majority of the error is occurring near the source. The reason for the errors in this area can be attributed to the voided node surrounding the source. What has been discovered is that the voided nodes are in fact acting more like "vacuum" nodes, in that the deflection of neutrons traveling through each node is grossly overestimated. Since neutron conservation is obeyed, this requires that more source neutrons be "sucked" into the void region to make the balance agree. This effect is mitigated somewhat as the angular expansion is increased and convergence to the reference solution is observable. Curiously, the iterative convergence problems also tend to lessen as the angular expansion is increased.

The flux solution right around the void region is where the largest errors are generally found. The flux solution significantly removed from the void region, however, is relatively accurate as indicated by Figure 15. Overall, the VARIANT-F solutions do have the correct general shape and the space-angle approximation employed is the source for the remaining discrepancies in the solutions.

The VARIANT-FI solutions to the Watanabe-Maynard benchmark are given in Figures 16, 17, 18, and 19 along with a TWODANT S_{12} solution. Similar to the VARIANT-F results, the void nodes in the VARIANT-FI formulation are also acting like "vacuum" nodes, but to a lesser degree. Comparing VARIANT-F P_1 to VARIANT-FI P_2

one can see that the integral formulation solution is generally more accurate. Further comparison of VARIANT-F P_3 to VARIANT-FI P_4 shows that the VARIANT-F solution is better than VARIANT-FI, however, this is believed to be a result of disadvantageous error cancellation for the integral formulation. Above P_4, VARIANT-FI on the average produces a much better flux solution to the benchmark than VARIANT-F. The most important difference between VARIANT-F and VARIANT-FI is that there were no difficulties with iterative convergence for the VARIANT-FI coding, which was not the case for VARIANT-F.

Figures 20 and 21 can be used to get a closer look at errors in the flux solution for VARIANT-FI and TWODANT. Figure 20 gives the magnitude of the calculated error (absolute value) for P_8, P_{12}, and P_{22} VARIANT-FI solutions along with TWODANT S_8 and S_{12} solutions along the diagonal traverse. Figure 21 gives the calculated error along the void traverse. From Figure 20, it is clear that the TWODANT code is accurate right at the source, but in the void region and near the vacuum boundary, the TWODANT solutions have substantial errors. By comparison, the VARIANT-FI results for the same order angular approximation have significant error near the source, but near the vacuum boundary, the error in the flux solution is small and generally less than 4%. From Figure 21, the VARIANT-FI solutions along the void traverse are very good with the flux typically less than 5% in error. As was the case in Figure 20, the TWODANT solutions have substantial errors typically exceeding 10%, which are unacceptable.

Overall, as the angular approximation is increased, the VARIANT-FI results clearly converge towards the reference solution while the differential form still has a considerable amount of error present in the void region. The P_{22} VARIANT-FI solution is very accurate with a maximum error of 1.5% inside of the void region and less than 1% outside of the void region indicating that the VARIANT-FI code can in fact obtain the correct solution given a high enough angular approximation. Compared to the AZMY benchmark, the VARIANT-FI solutions are slightly less accurate, but this can be attributed to simple fact that the void benchmark is a more difficult transport problem. When compared to the TWODANT solution, the VARIANT-FI solutions with the same angular order are much better. When performing the discrete ordinates solutions to this benchmark, angular quadratures around S_{32} (level symmetric) or SLC_{16} are typically required to obtain solutions similar to those of the S_8 VARIANT-FI solutions. To obtain discrete ordinate solutions that are as accurate as the P_{22} VARIANT-FI, angular quadratures on the order of S_{64} or SLC_{32} have been used.

VII.c Modified Watanabe-Maynard Problem 2

As was mentioned earlier, the problem 2 (P2) cross sections in Figure 2 were introduced to make the void benchmark similar to that of the AZMY benchmark and thus more difficult. Figures 22, 23, 24, and 25 give the solutions for the four flux traverses obtained with VARIANT-F. As can be seen, three solutions are again given for the P_9 approximation in each figure with the numbers in parenthesis indicating the total number

of iterations used in the problem solution. For this problem the iterative convergence was even worse, typically resulting in error an order of magnitude higher at 2000 iterations. However, as was the case in the preceding benchmark, the VARIANT-F solutions are converging.

In Figures 22 through 25, the majority of the error is occurring near the source. The reason for the errors can again be attributed to the voided nodes acting like "vacuum" nodes. In this case, however, the flux solution near the vacuum boundary is very close because of the small scattering component. The spherical harmonics approaches typically do well for problems such as these while discrete ordinates do not. Overall, the VARIANT-F solutions do have the correct shape, but the space-angle approximation employed is simply not sufficient.

The VARIANT-FI solutions to the Watanabe-Maynard benchmark are given in Figures 26, 27, 28, and 29 along with a TWODANT S_{12} solution. In all four Figures, it is clear that as the angular approximation is increased, the VARIANT-FI results converge towards the reference solution. As expected, though, compared to the preceding two benchmarks, the VARIANT-FI solutions are slightly less accurate (a more difficult transport problem). In general, the P_{12} and P_{22} VARIANT-FI solutions are fairly accurate with both flux solutions having the correct flux shape. Comparing to the TWODANT solutions, the VARIANT-FI solutions with the same angular order are again much better.

Figure 30 gives the magnitude of the calculated error for P_8, P_{12}, and P_{22} VARIANT-FI solutions along with TWODANT S_8 and S_{12} solutions along the diagonal traverse. Figure 21 gives the calculated error along the void traverse. The VARIANT-FI solutions have a majority of the error near the void region, but relatively little near the vacuum boundary. The VARIANT-FI solutions are clearly worse than that seen in problem 1, with the P_{12} solution having a maximum error of 10% and the P_{22} solution with a maximum error of 4%. Once again, the TWODANT code is accurate at the source, but everywhere else it is generally very inaccurate. The most severe errors of course occur near the vacuum boundary condition which can be seen in Figure 29. Overall, the inaccuracies in the P_{22} solution can be considered understandable given the extreme nature of the benchmark. However, it is clear that both the TWODANT and VARIANT-FI formulations need additional space-angle refinement before accurate (<1% error) solutions are obtained.

VIII. Computational Timing and Future Work

The most significant information to mention about the differences between the differential and integral formulations is the relative computational effort required to obtain the response matrices. Specifically, the computational burden lays in the inversion of the $\mathbf{A}$ and the $\mathbf{A}_\Omega$ matrices and numerical determination of Eq. (62). The outer iteration procedure can be made similar to the second order differential form and thus acceleration techniques, which were not applied in this work, are available [11].

The dimension of **A** in the differential formulation is equal to the number of angular degrees of freedom multiplied by the number of spatial degrees of freedom used to approximate the flux. Because of memory limitations, the 3-D second order differential formulation presently employed in VARIANT is limited to a maximum P_{11} angular approximation on modern computing technology. A practical limitation for reactor physics applications is P_7. For the first order differential formulation, this equates to constraining the maximum angular approximation to P_7 with a practical limitation of about P_3, possibly P_5.

Although these estimates depend greatly on the number of groups and number of unique nodes, clearly the use of the first order formulation is expensive. Fortunately, the first and second order differential formulations are compatible and the size of void regions in reactor geometries is expected to be relatively small. From the solutions given in the three benchmark problems of this work and the fact that the solutions obtained using VARIANT-F are reasonably good, it is justifiable to implement the first order differential formulation within VARIANT. At a minimum, the exploration of the compatibility of the first and second order differential methods needs to be investigated thoroughly to see what effect it has upon the solution accuracy.

For the integral formulation, the dimension of $\mathbf{A}_\Omega$ is equal to the number of spatial degrees of freedom used to approximate the flux. The major expense of the method comes from the order of the angular quadrature used to obtain the response matrices. At present, a minimum SLC_{16} quadrature is employed (~S_{36}), regardless of whether it is needed (no check is performed on the accuracy of the angular integrals). The side effect of course is unnecessary computational expense. The minimum required quadrature is $N+2$ where N is the P_N order applied along the boundary. The impact of the quadrature approximation is one area of this method that needs to be investigated more thoroughly.

For the most part, the first and second order integral formulations are limited by the time required to solve the outer iterations rather than a memory requirement or the computational time needed for the response matrix formation. This is due to the fact that the acceleration techniques developed for the second order differential form do not apply well for the integral methods (odd P_N and even P_N are not equivalent). As a consequence, to implement the method in VARIANT requires either the investigation of odd P_N boundary conditions (they appear possible) or the search for more appropriate acceleration techniques. In terms of accuracy, clearly the integral formulation does a better job on voided regions than the differential formulation.

IX. Conclusions

The overall conclusion that can be reached for all three benchmarks is that the new formulations can treat void regions. For the differential formulation, it is clear from the numerical results that only the bounded $\boldsymbol{\varphi}_\gamma$ interface condition produces acceptable results for odd P_N boundary conditions. Also, from the voided node benchmarks, it is clear that the Rumyantsev angular interface set is the appropriate set to use. The

solutions obtained using VARIANT-F proved to have the correct flux shape, but an insufficient space-angle approximation and slow convergence in the outer iterations prevent the differential formulation from obtaining accurate solutions. Contrary to this behavior, all three benchmarks were solved rather well using the first order integral formulation. The first two benchmarks were solved especially well with the solutions for the third benchmark considered sufficient under the circumstances.

From a researcher's viewpoint, it is quite gratifying to be able to demonstrate a method capable of treating void regions that is based on the spherical harmonics method. To our knowledge, this is the first time this has been achieved. Most importantly, the new formulations are compatible with their second order counterparts available in the VARIANT code. Finally, the main advantage of the spherical harmonics method over that of discrete ordinates methods was indicated by the lack of ray effects in the flux solution.

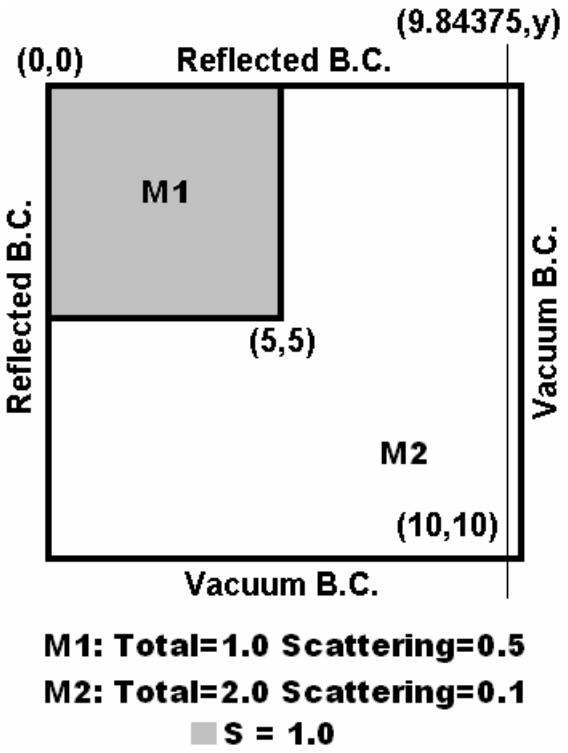

Figure 1 AZMY Benchmark Geometry

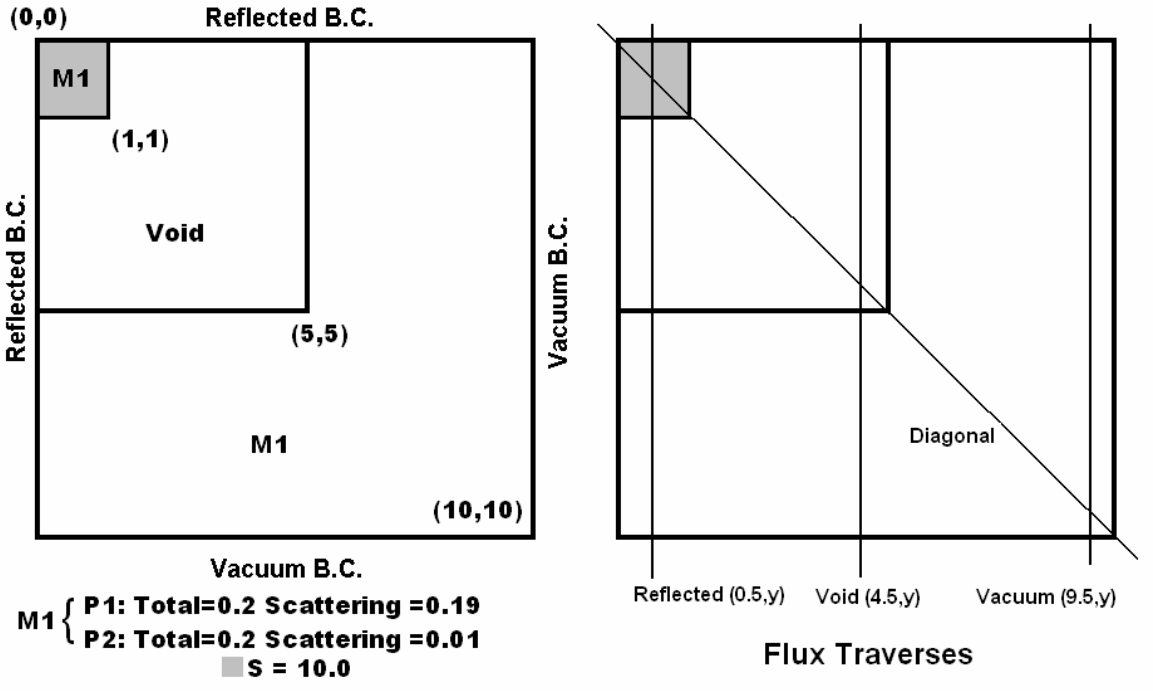

Figure 2. Modified Watanabe-Maynard Benchmark Geometry

Table I. Interface Conditions for the First Order Differential Method

	a	***b***	**Physical Interpretation**
Bounded φ_γ	2.0	0.0	$\frac{1}{2}a\varphi_\gamma + b\chi_\gamma = \varphi_\gamma$
Bounded χ_γ	0.0	1.0	$\frac{1}{2}a\varphi_\gamma + b\chi_\gamma = \chi_\gamma$
Bounded $\mathbf{j}^+$	0.5	0.5	$\frac{1}{2}a\varphi_\gamma + b\chi_\gamma = \mathbf{j}^+$
Bounded $\mathbf{j}^-$	0.5	-0.5	$\frac{1}{2}a\varphi_\gamma + b\chi_\gamma = \mathbf{j}^-$

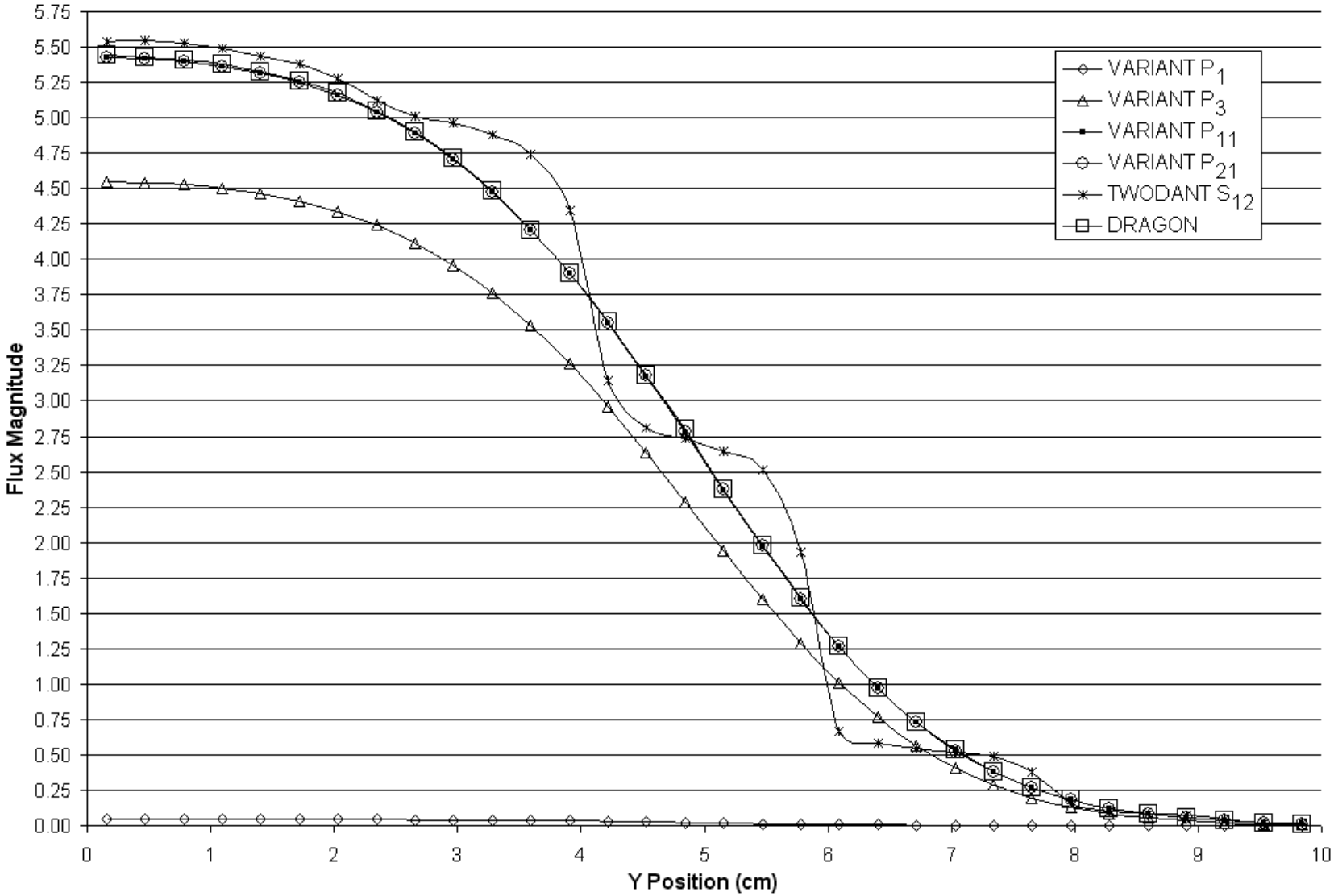

Figure 3. VARIANT, DRAGON, and TWODANT solutions to the AZMY Benchmark

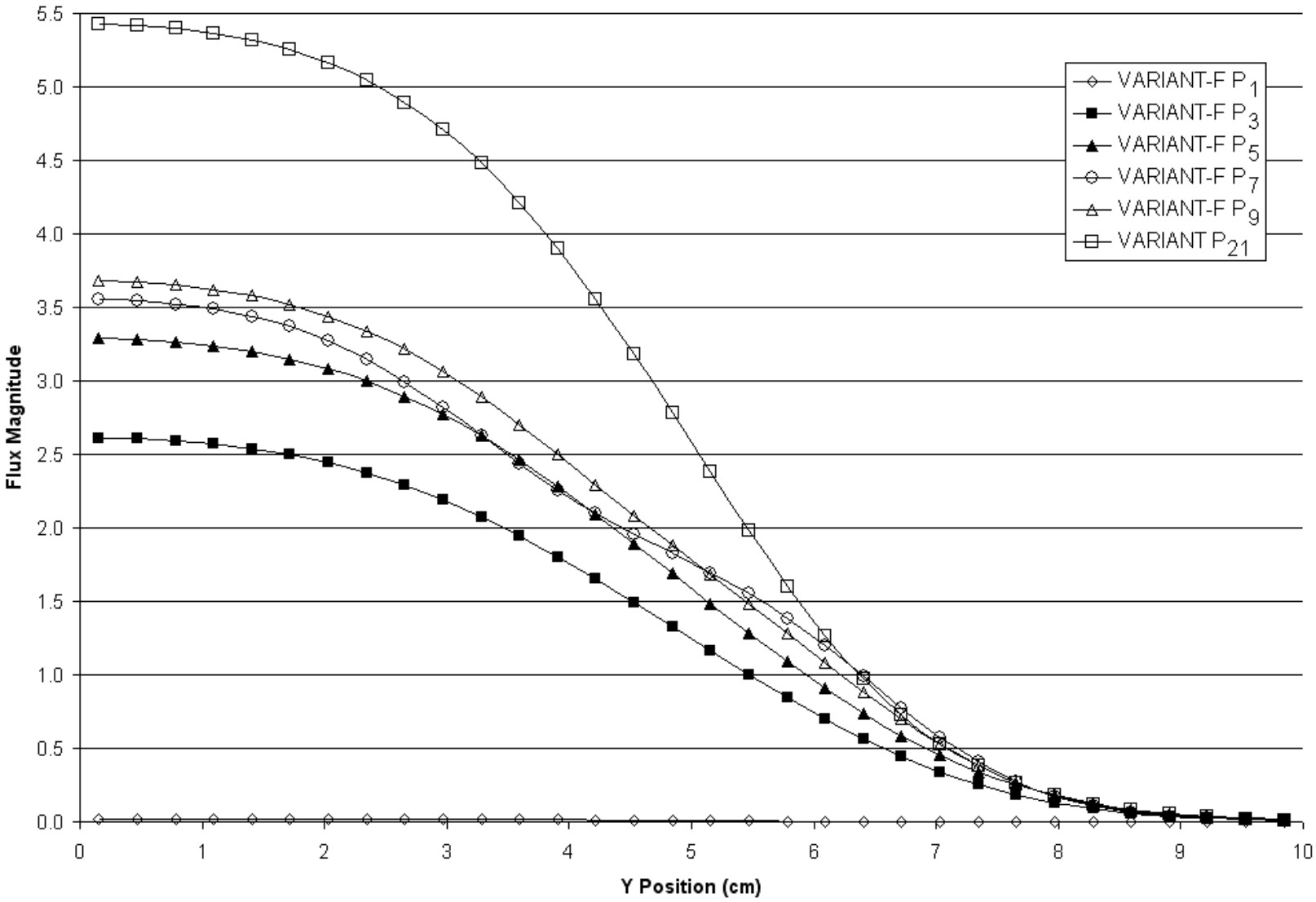

Figure 4. Bounded φ_γ, LI Set, VARIANT-F Solutions to the AZMY Benchmark

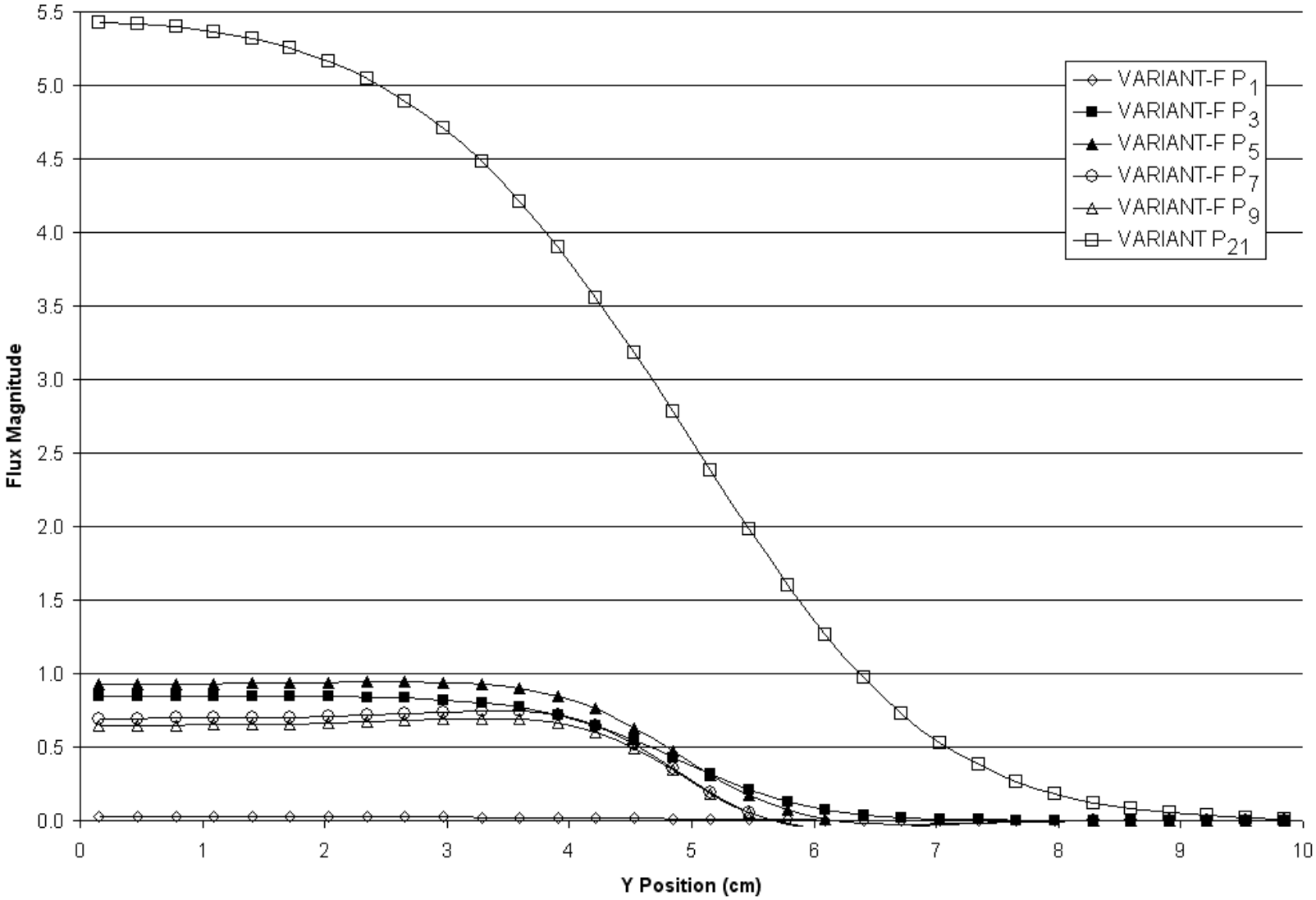

Figure 5. Bounded χ_γ, LI Set, VARIANT-F Solutions to the AZMY Benchmark

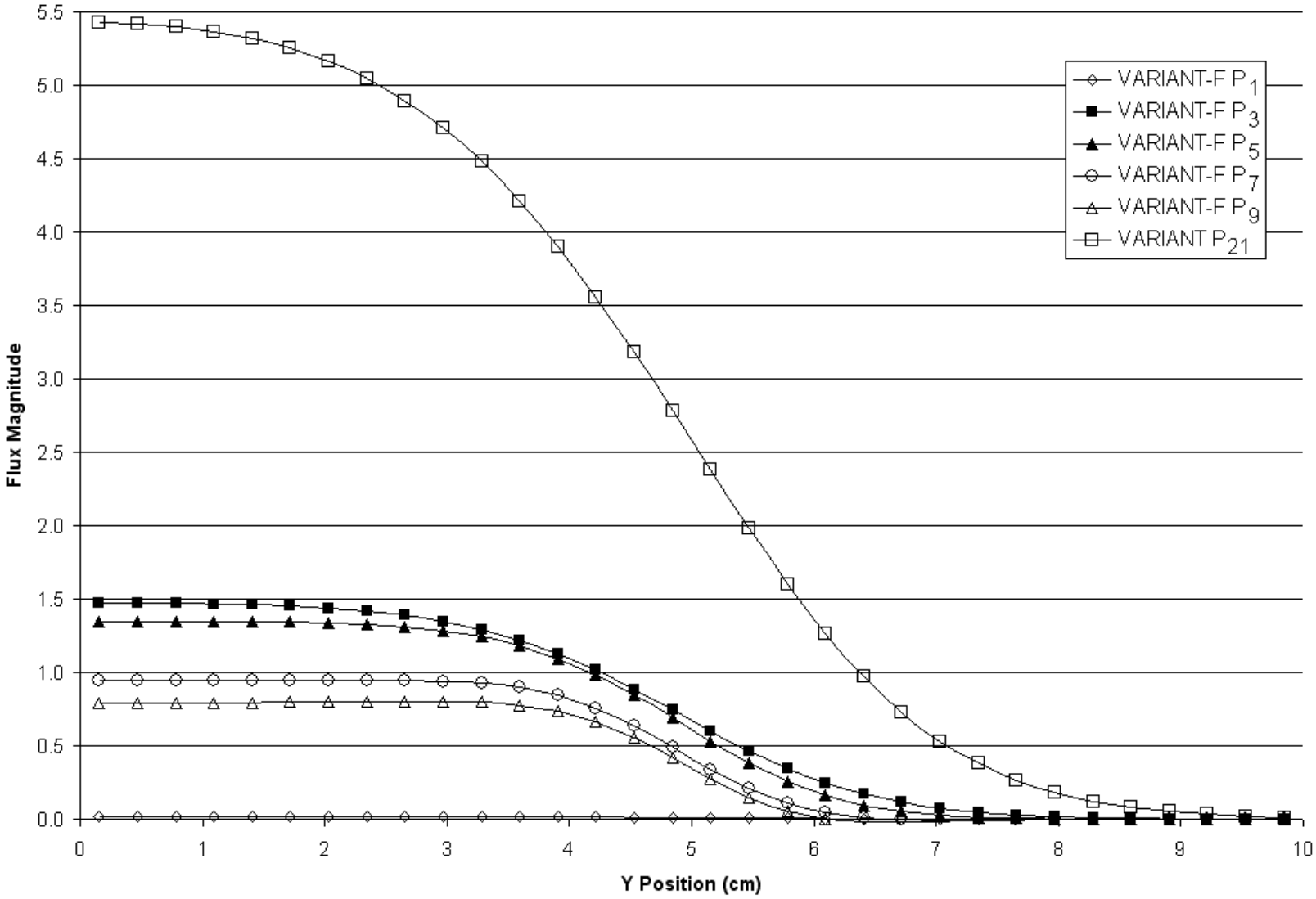

Figure 6. Bounded j^+, LI Set, VARIANT-F Solutions to the AZMY Benchmark

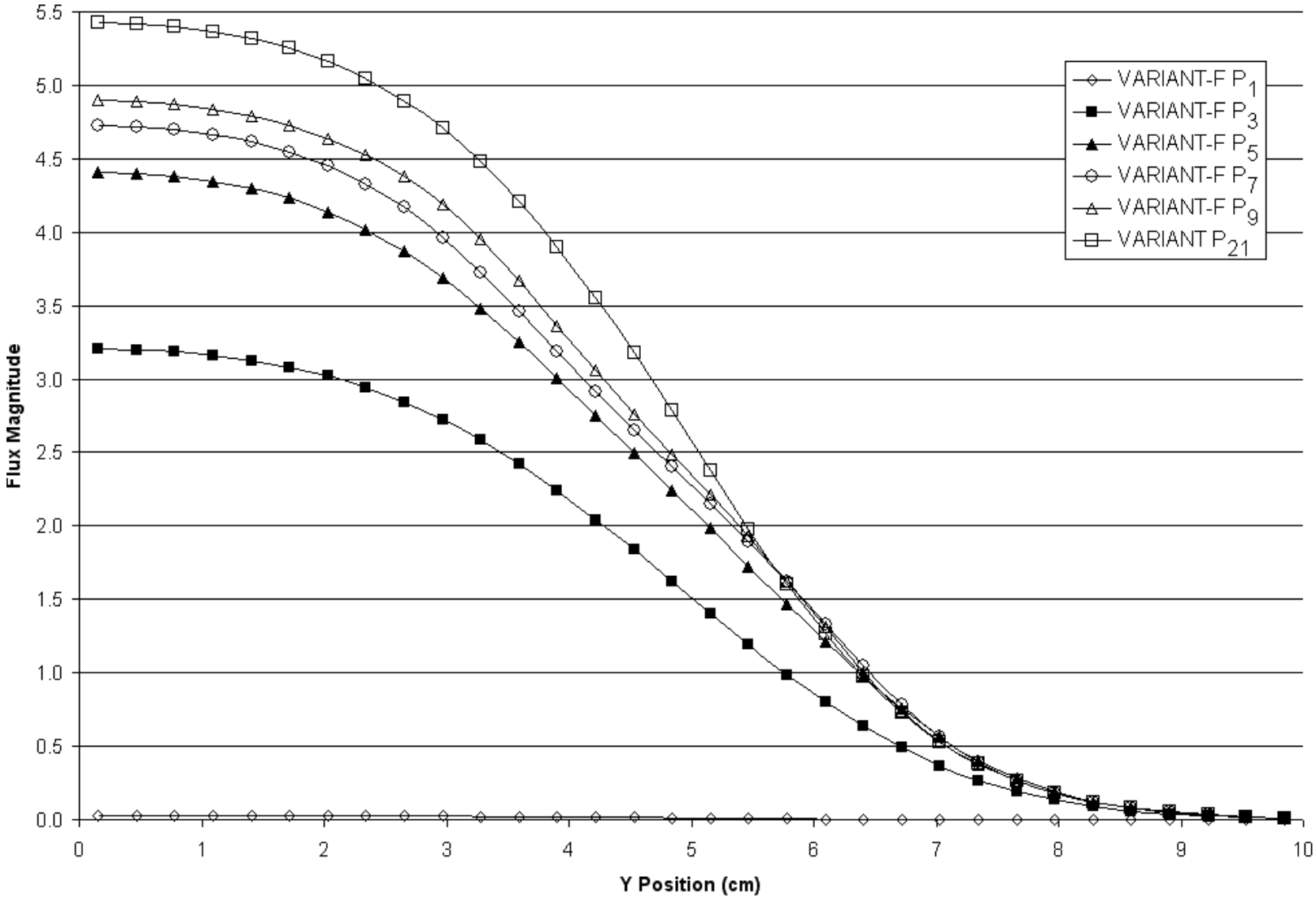

Figure 7. Bounded φ_γ, Rumyantsev Set, VARIANT-F Solutions to the AZMY Benchmark

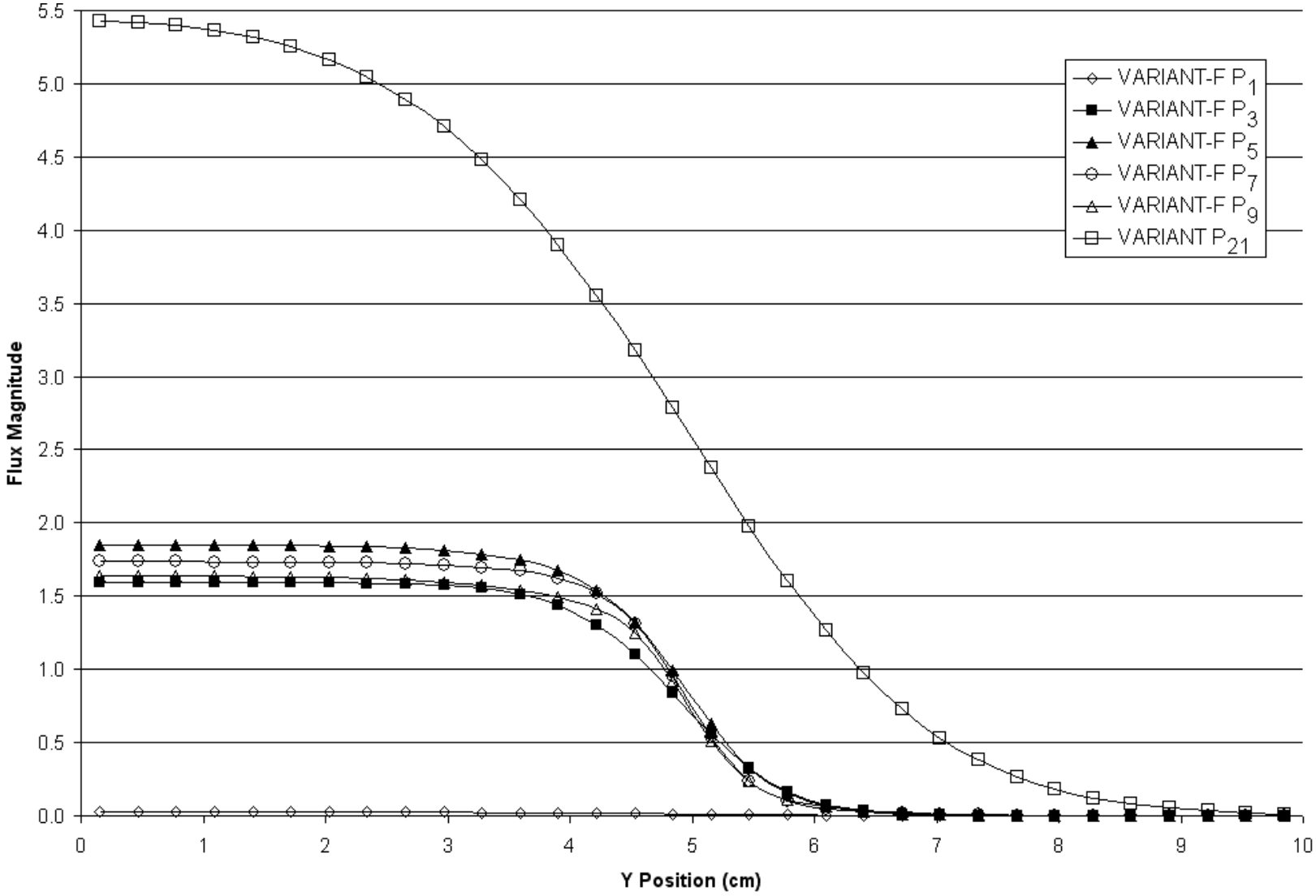

Figure 8. Bounded χ_γ, Rumyantsev Set, VARIANT-F Solutions to the AZMY Benchmark

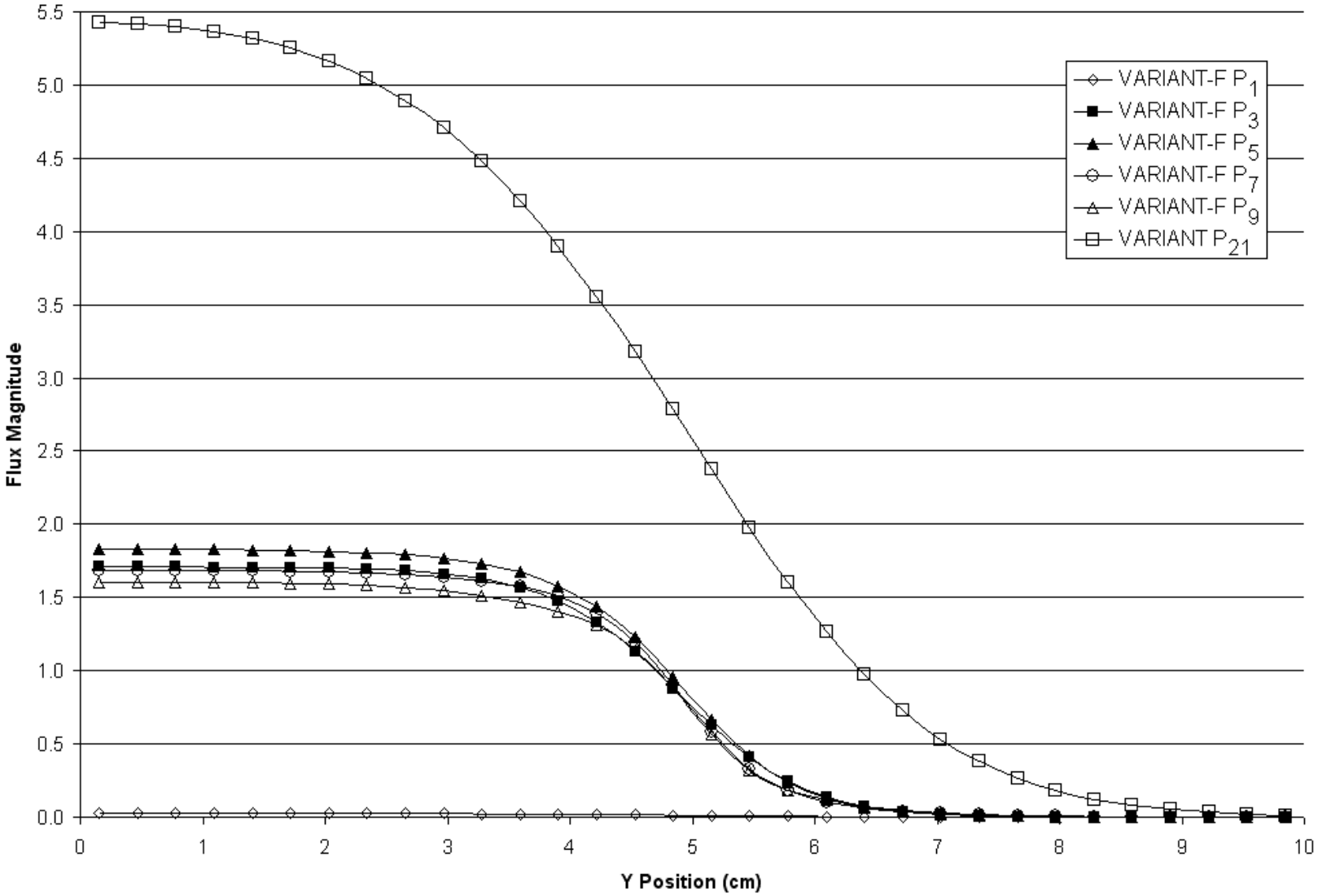

Figure 9. Bounded j^{+}, Rumyantsev Set, VARIANT-F Solutions to the AZMY Benchmark

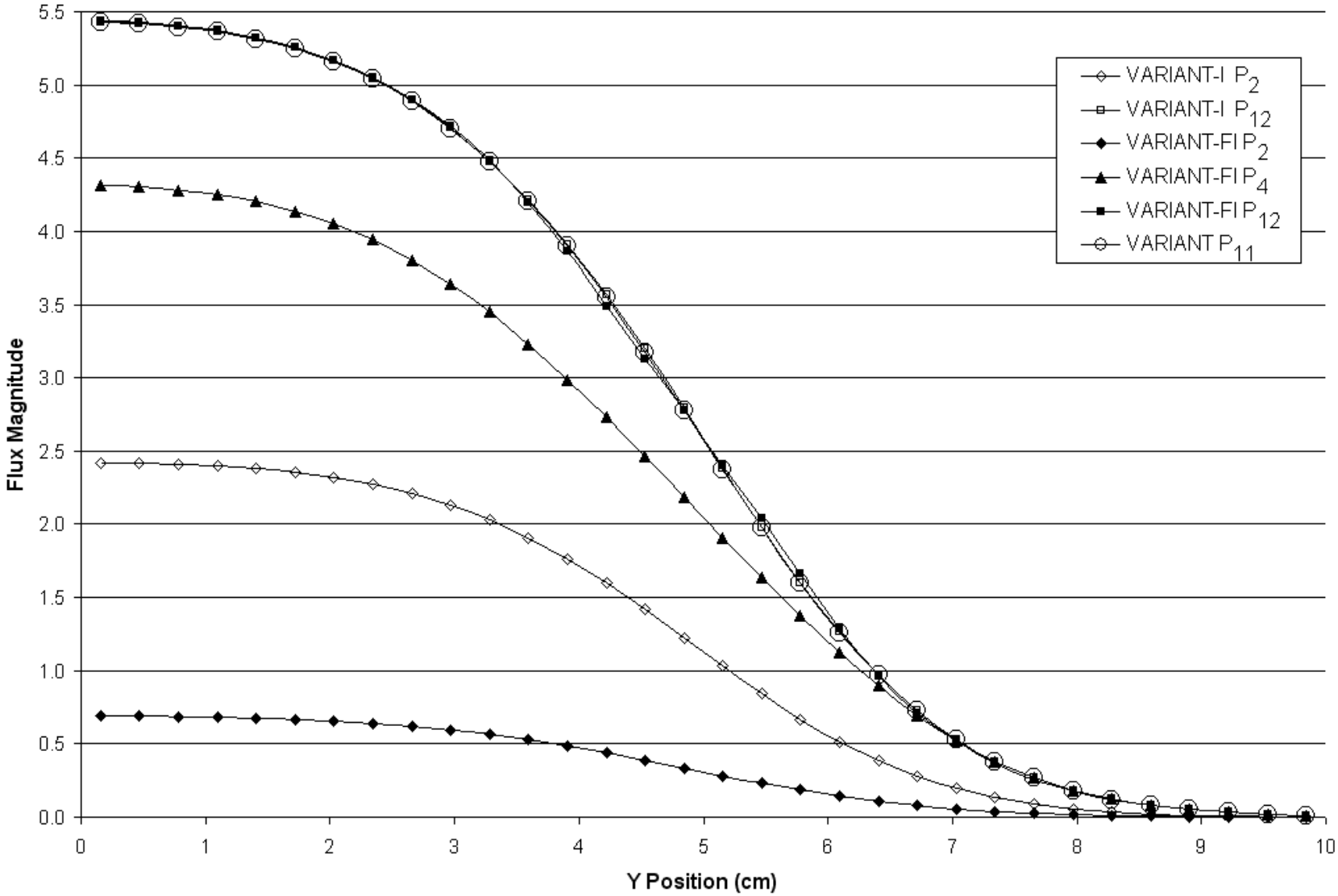

Figure 10. VARIANT-I and VARIANT-FI Solutions to the AZMY Benchmark

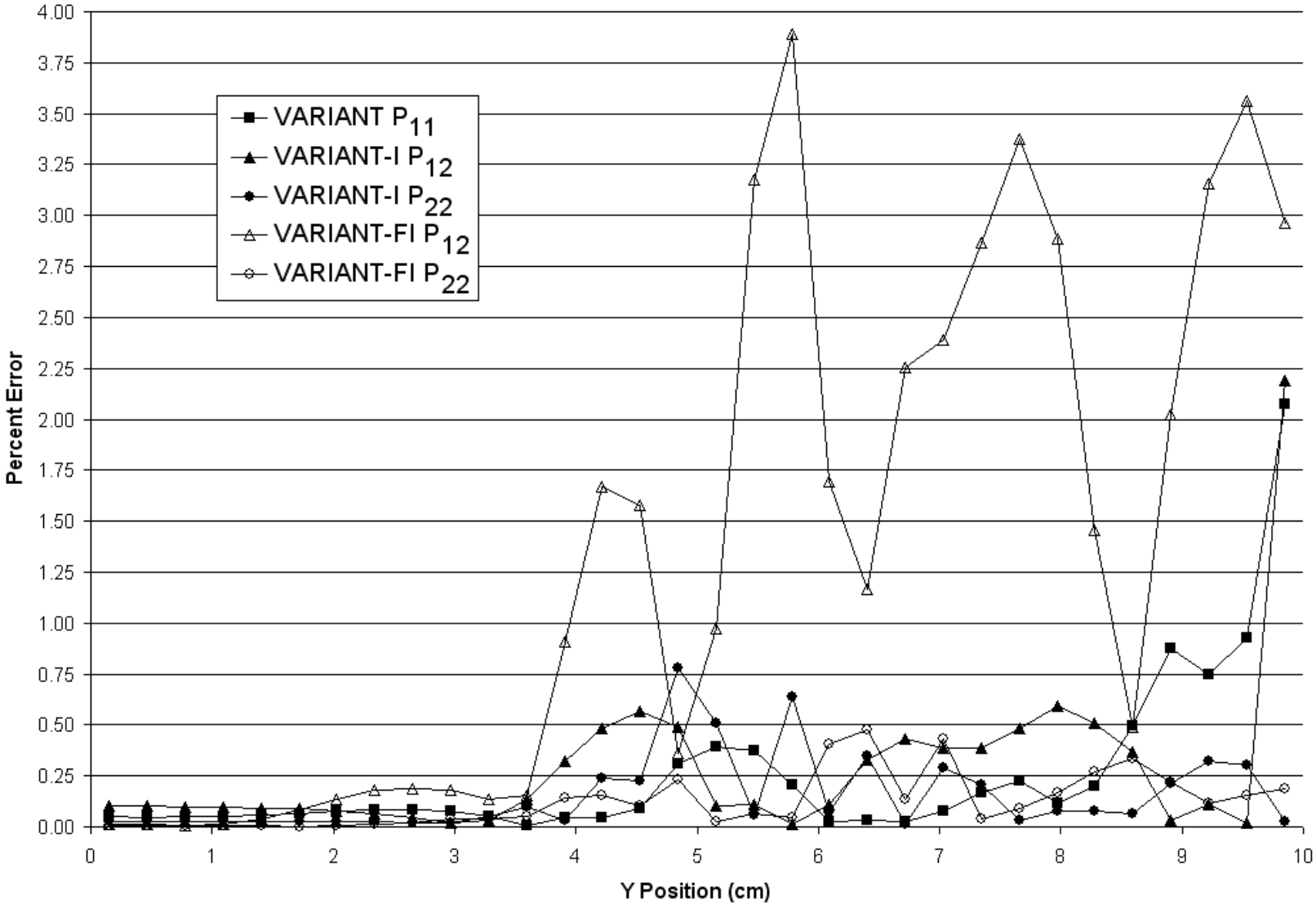

Figure 11. Absolute VARIANT, VARIANT-I, and VARIANT-FI Errors for the AZMY Benchmark

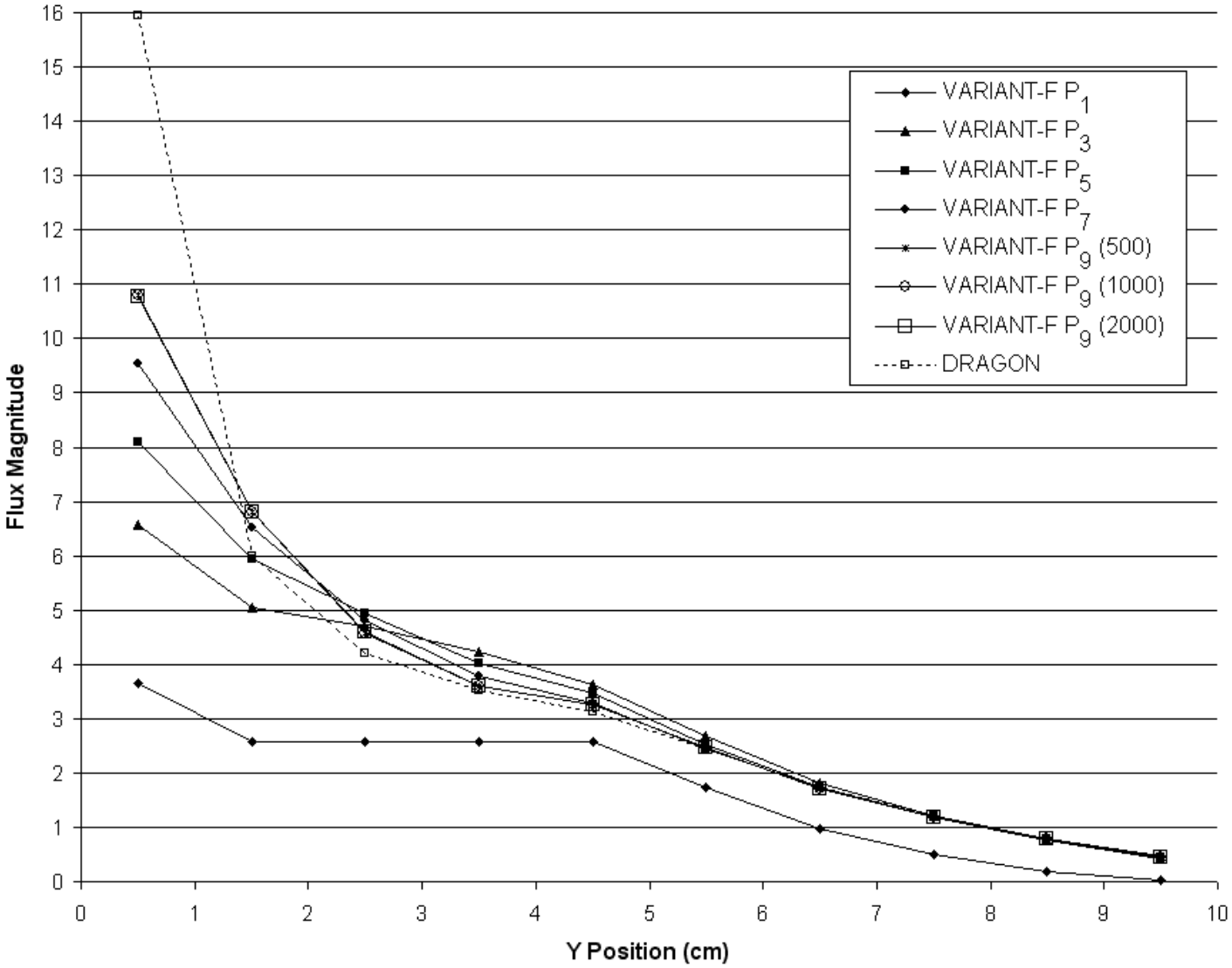

Figure 12. VARIANT-F Solutions to the Watanabe-Maynard Benchmark Problem 1, Diagonal Traverse

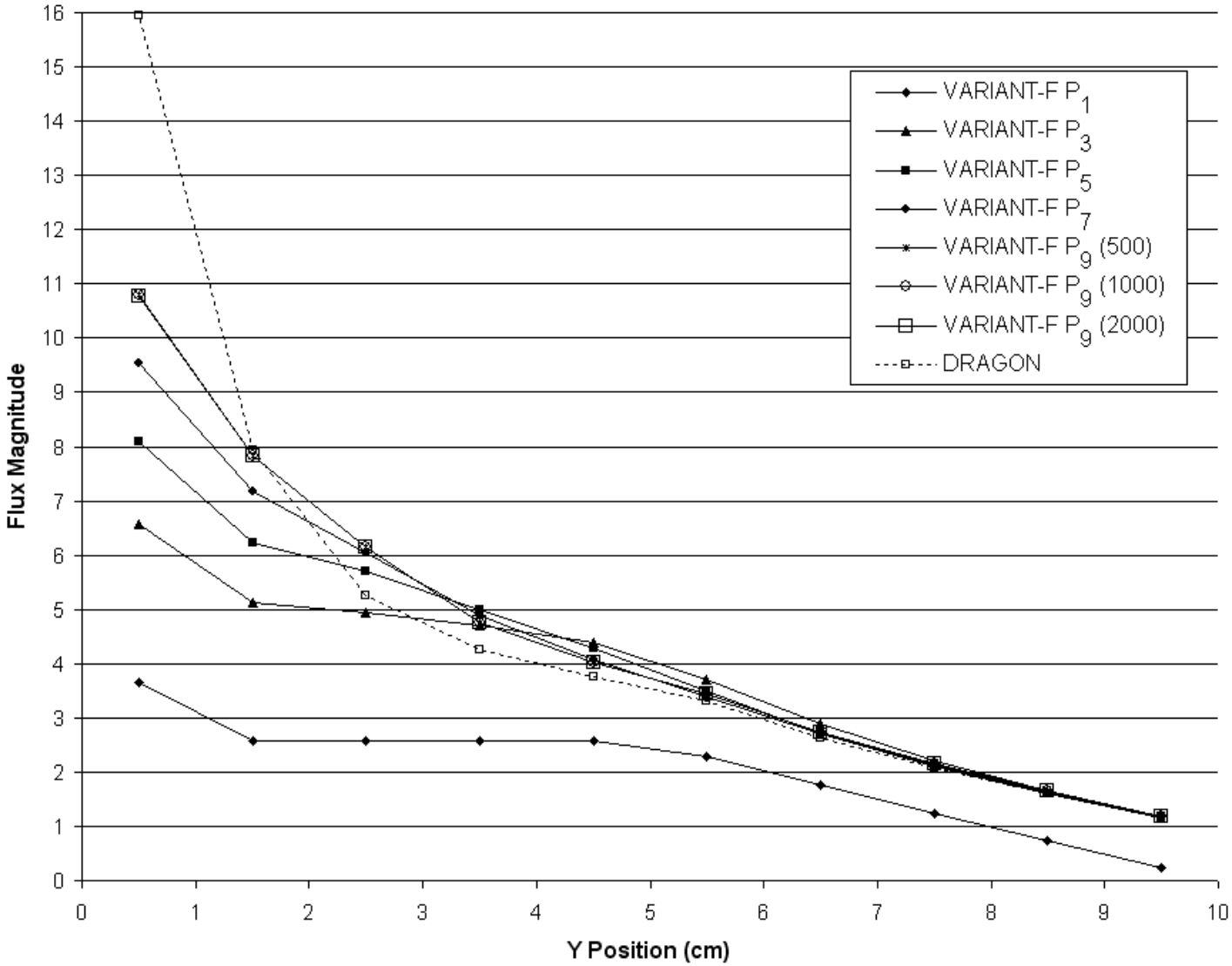

Figure 13. VARIANT-F Solutions to the Watanabe-Maynard Benchmark Problem 1, Reflected Traverse

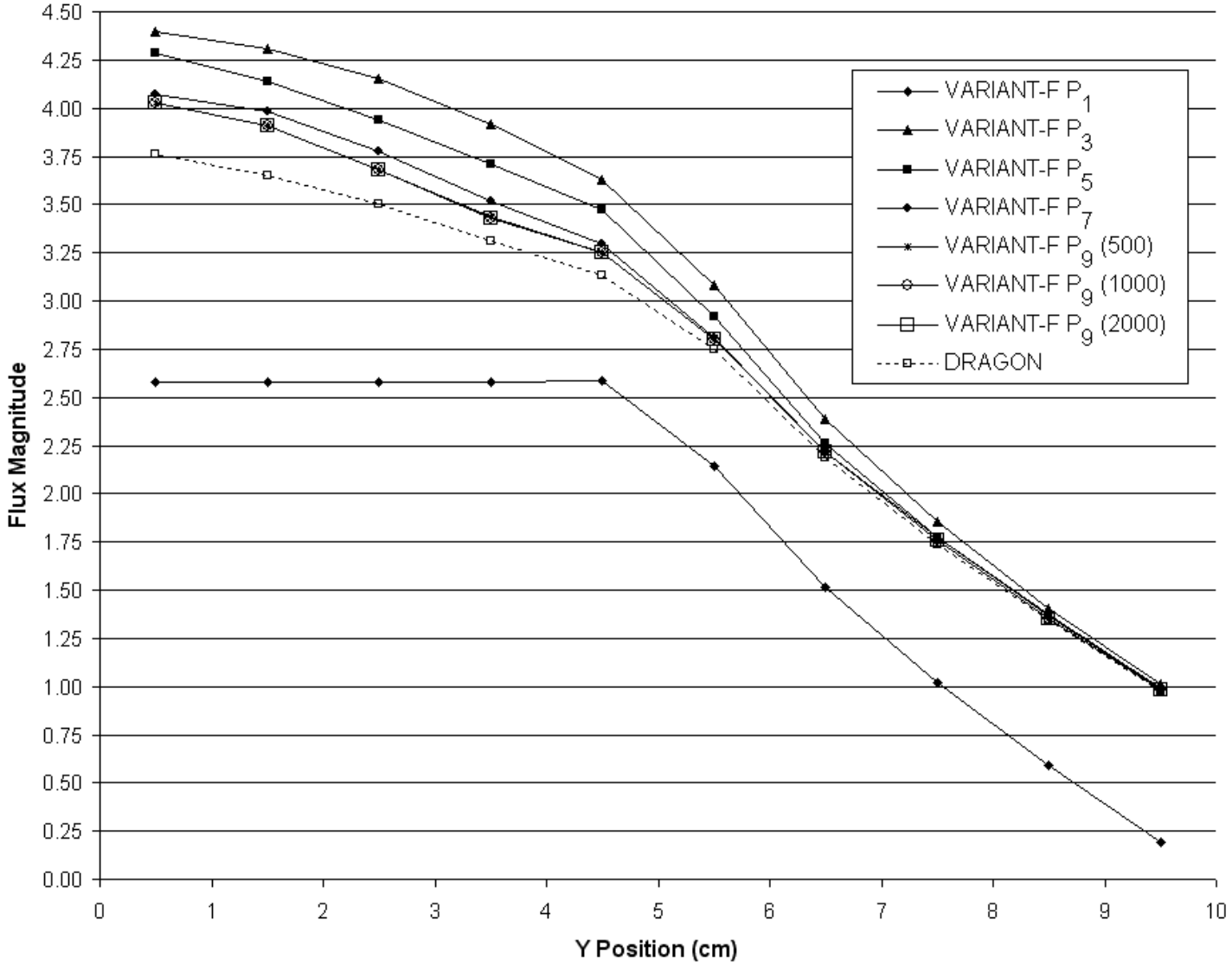

Figure 14. VARIANT-F Solutions to the Watanabe-Maynard Benchmark Problem 1, Void Traverse

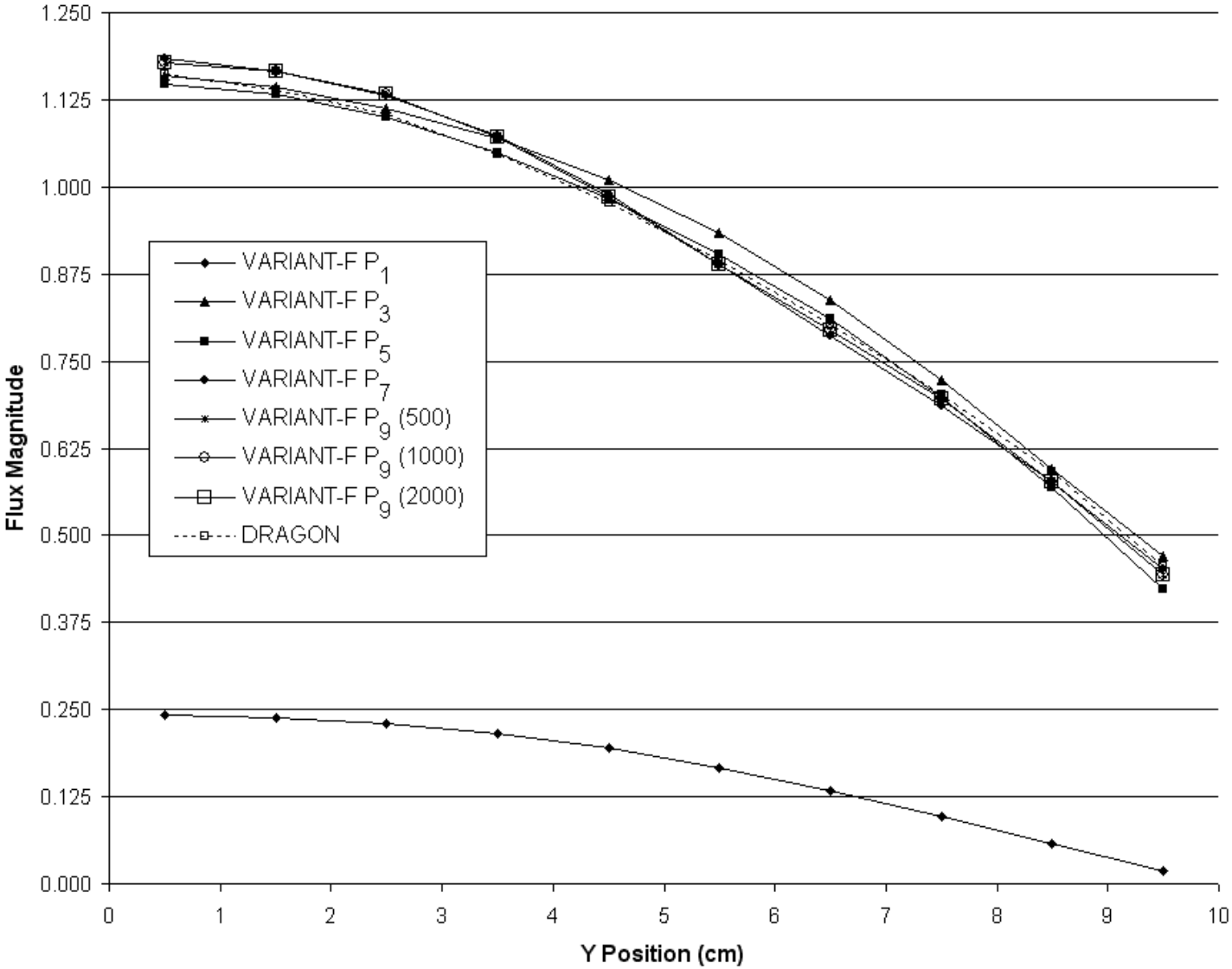

Figure 15. VARIANT-F Solutions to the Watanabe-Maynard Benchmark Problem 1, Vacuum Traverse

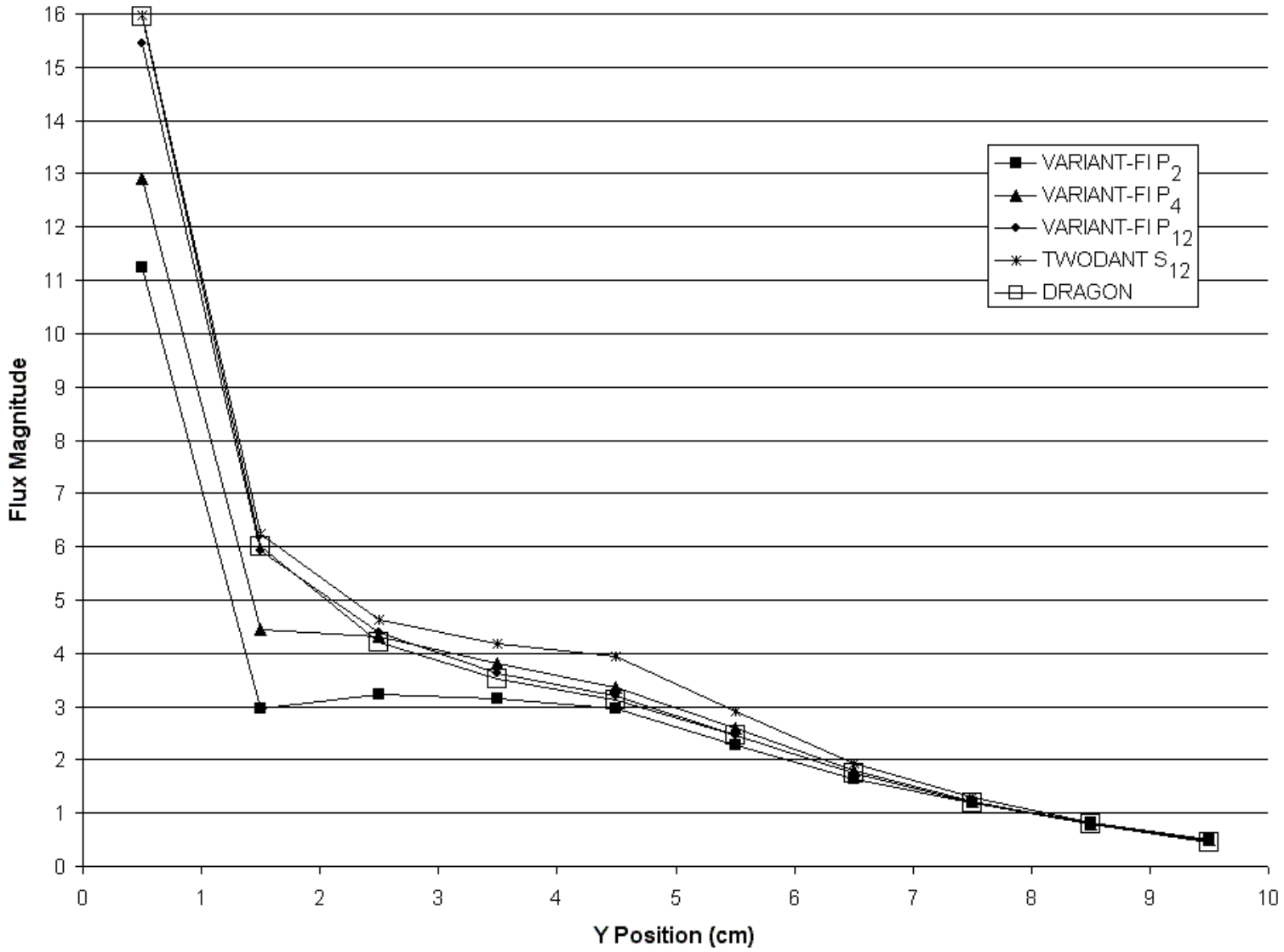

Figure 16. VARIANT-FI Solutions to the Watanabe-Maynard Benchmark Problem 1, Diagonal Traverse

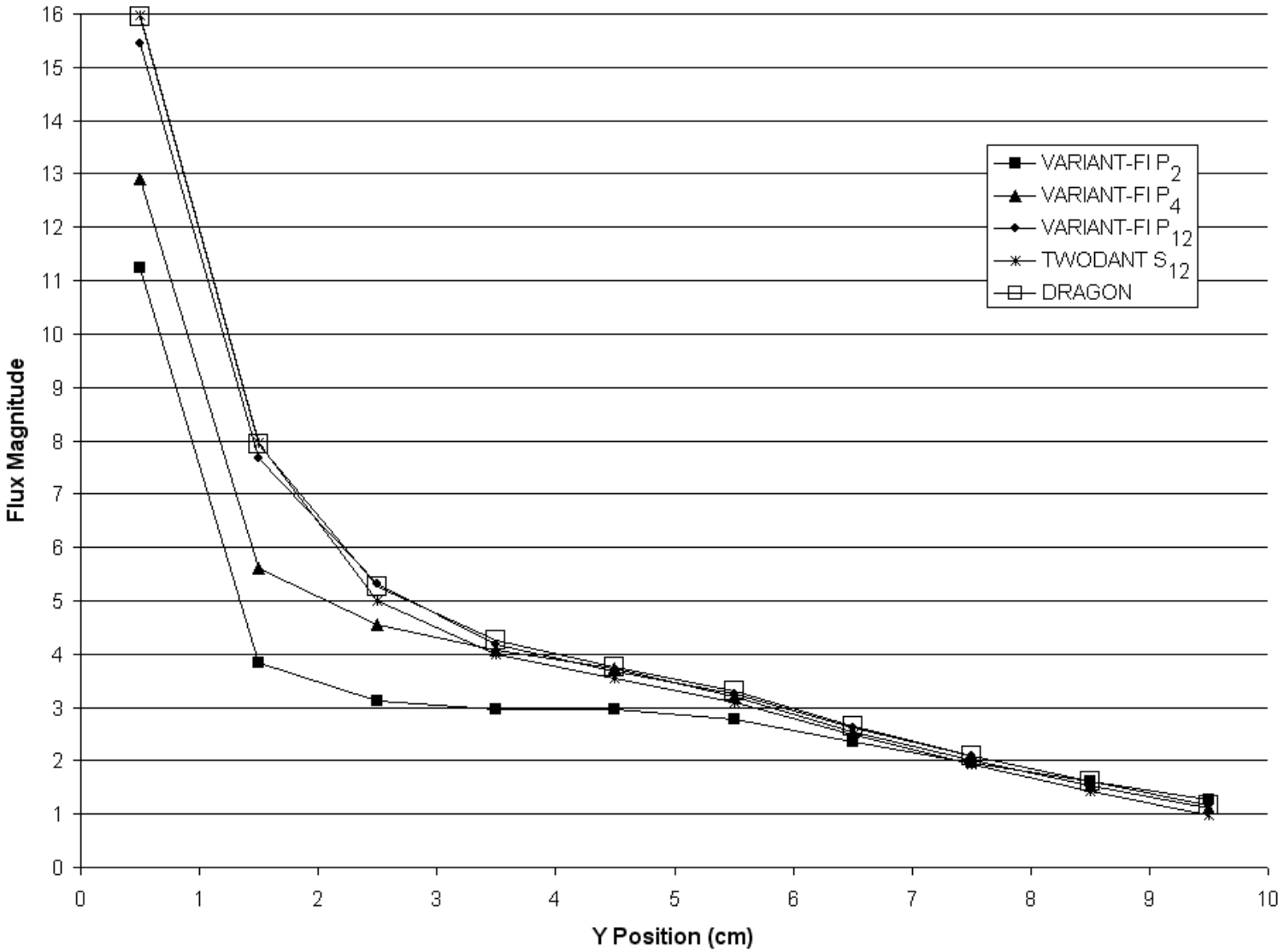

Figure 17. VARIANT-FI Solutions to the Watanabe-Maynard Benchmark Problem 1, Reflected Traverse

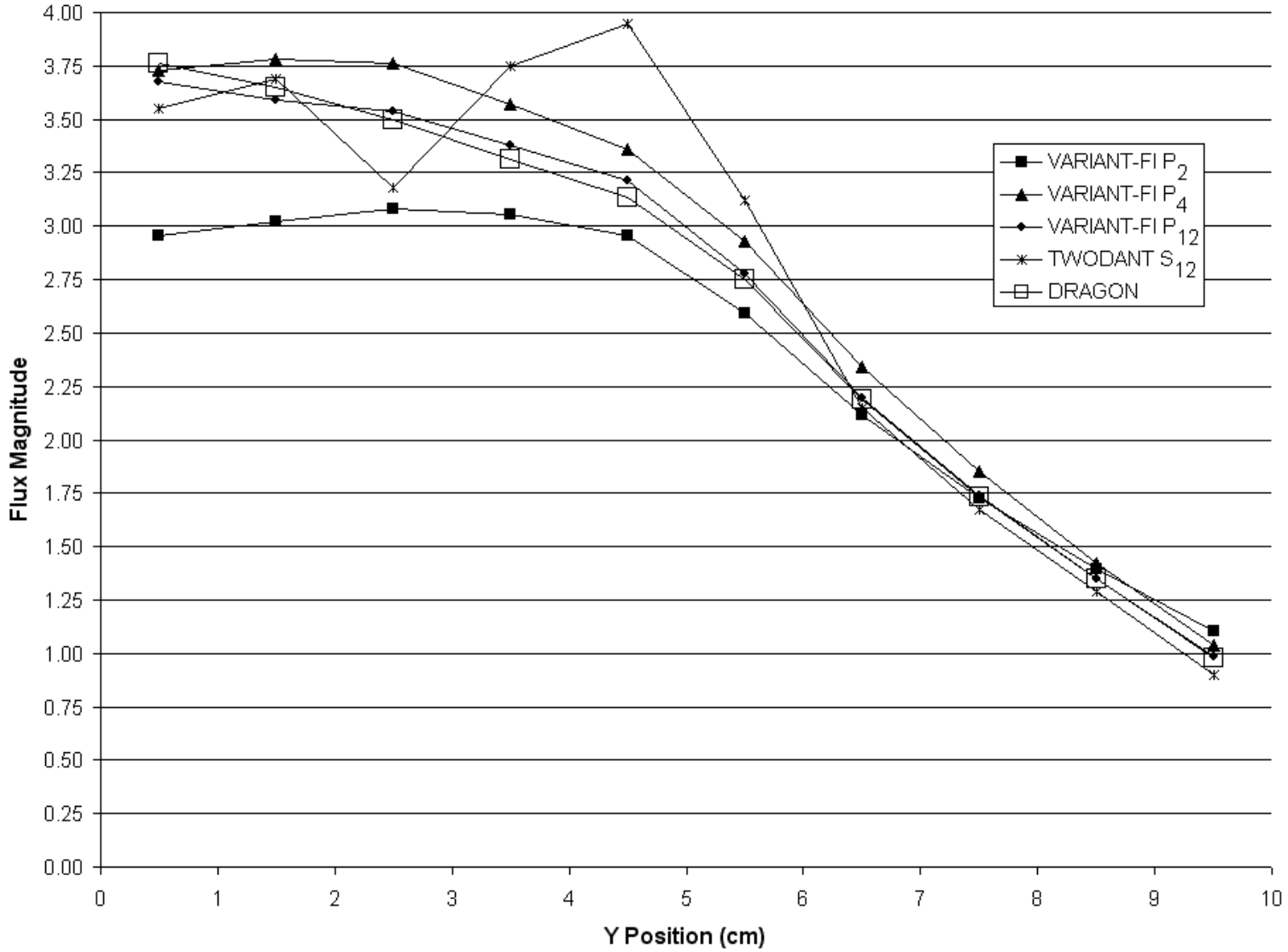

Figure 18. VARIANT-FI Solutions to the Watanabe-Maynard Benchmark Problem 1, Void Traverse

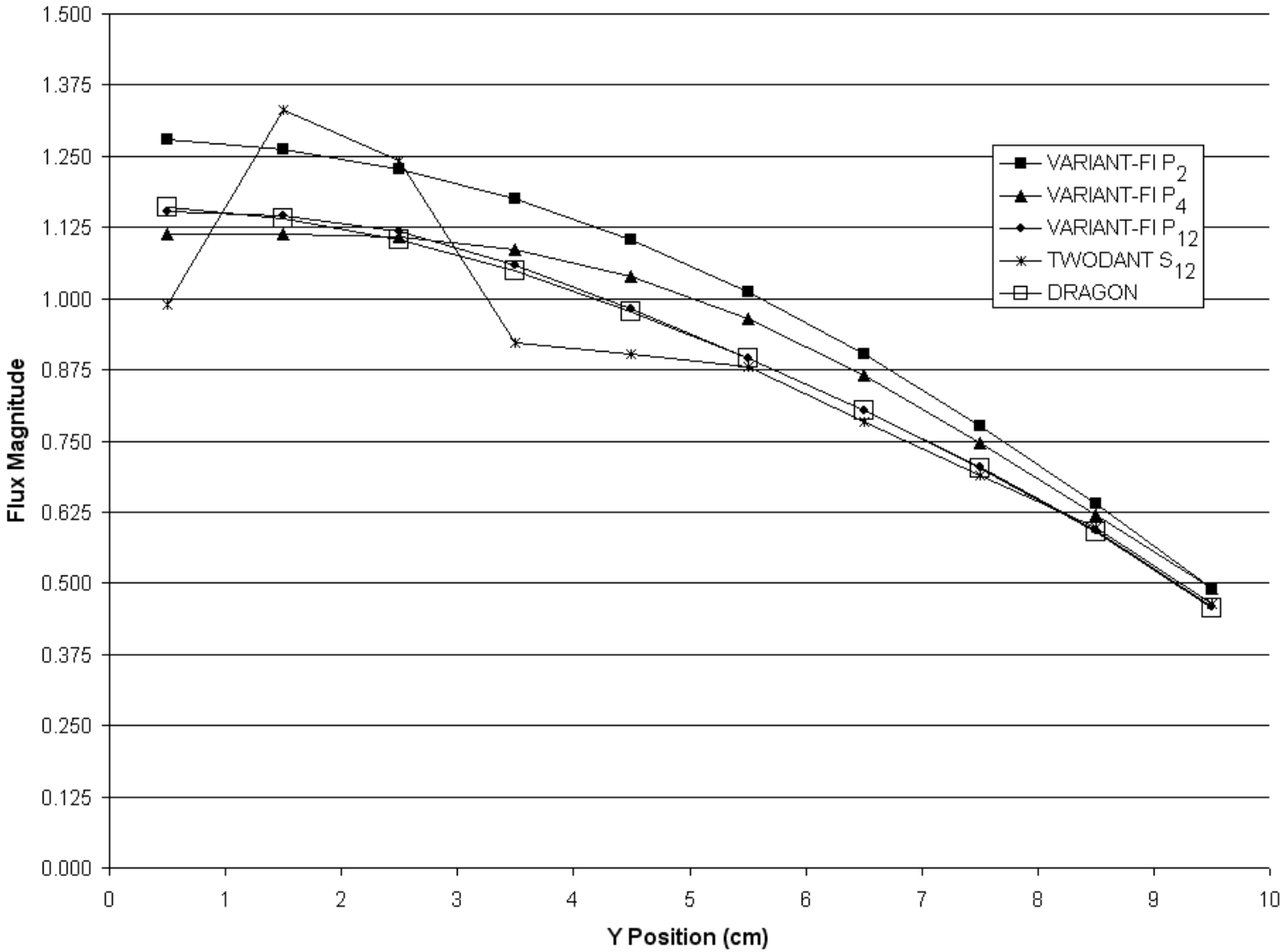

Figure 19. VARIANT-FI Solutions to the Watanabe-Maynard Benchmark Problem 1, Vacuum Traverse

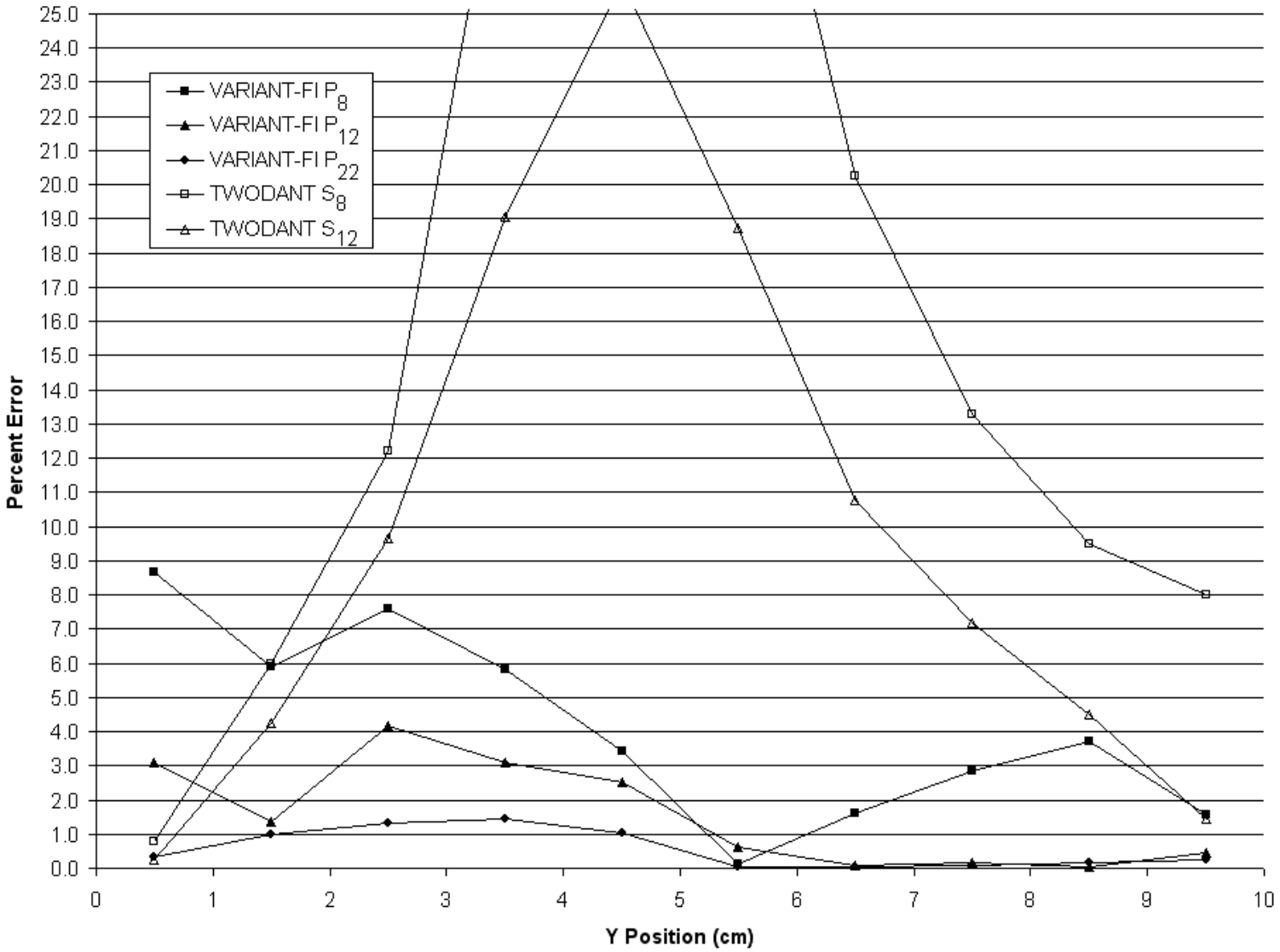

Figure 20. VARIANT-FI and TWODANT Error for the Watanabe-Maynard Benchmark Problem 1, Diagonal Traverse

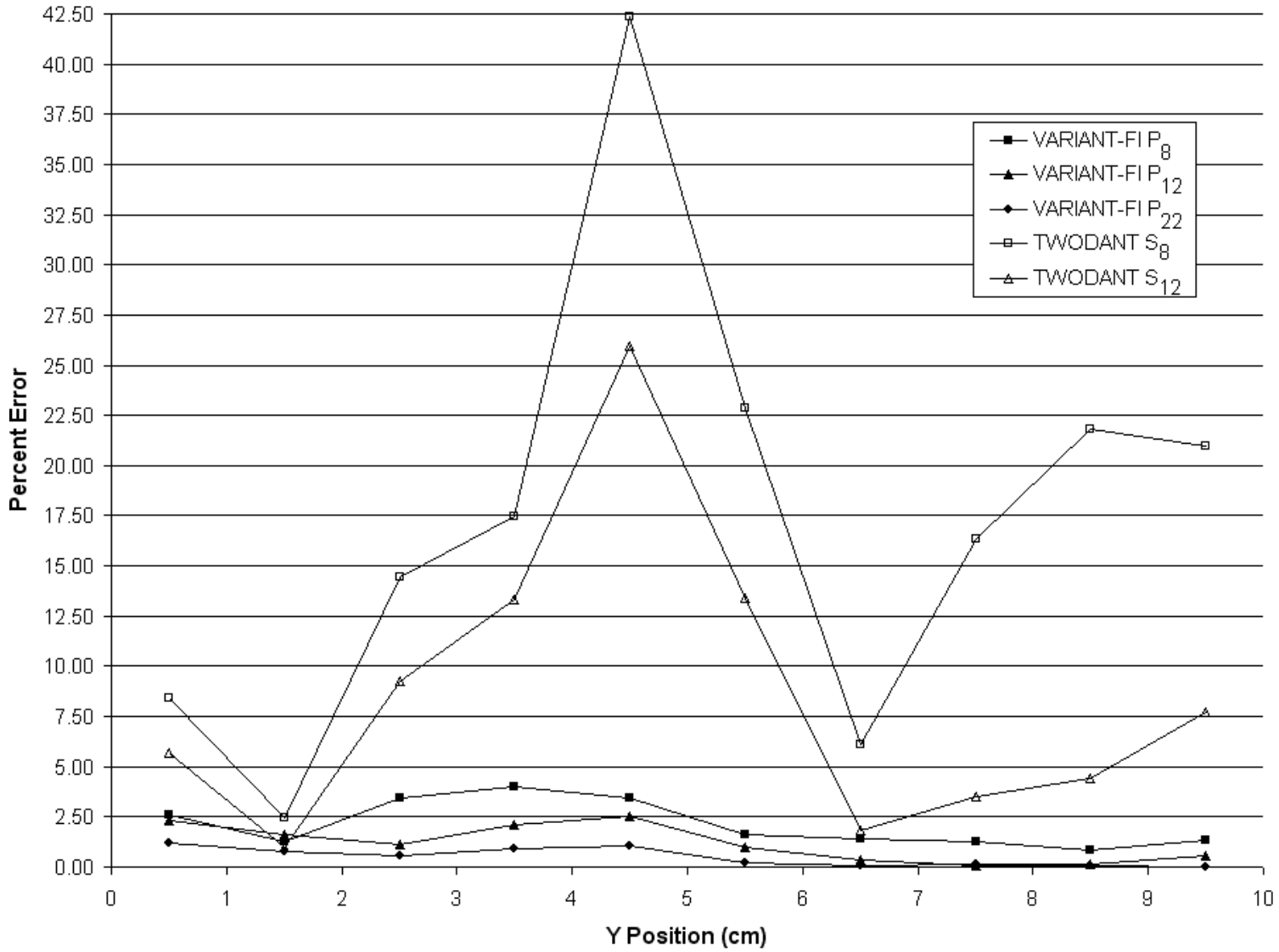

Figure 21. VARIANT-FI and TWODANT Error for the Watanabe-Maynard Benchmark Problem 1, Void Traverse

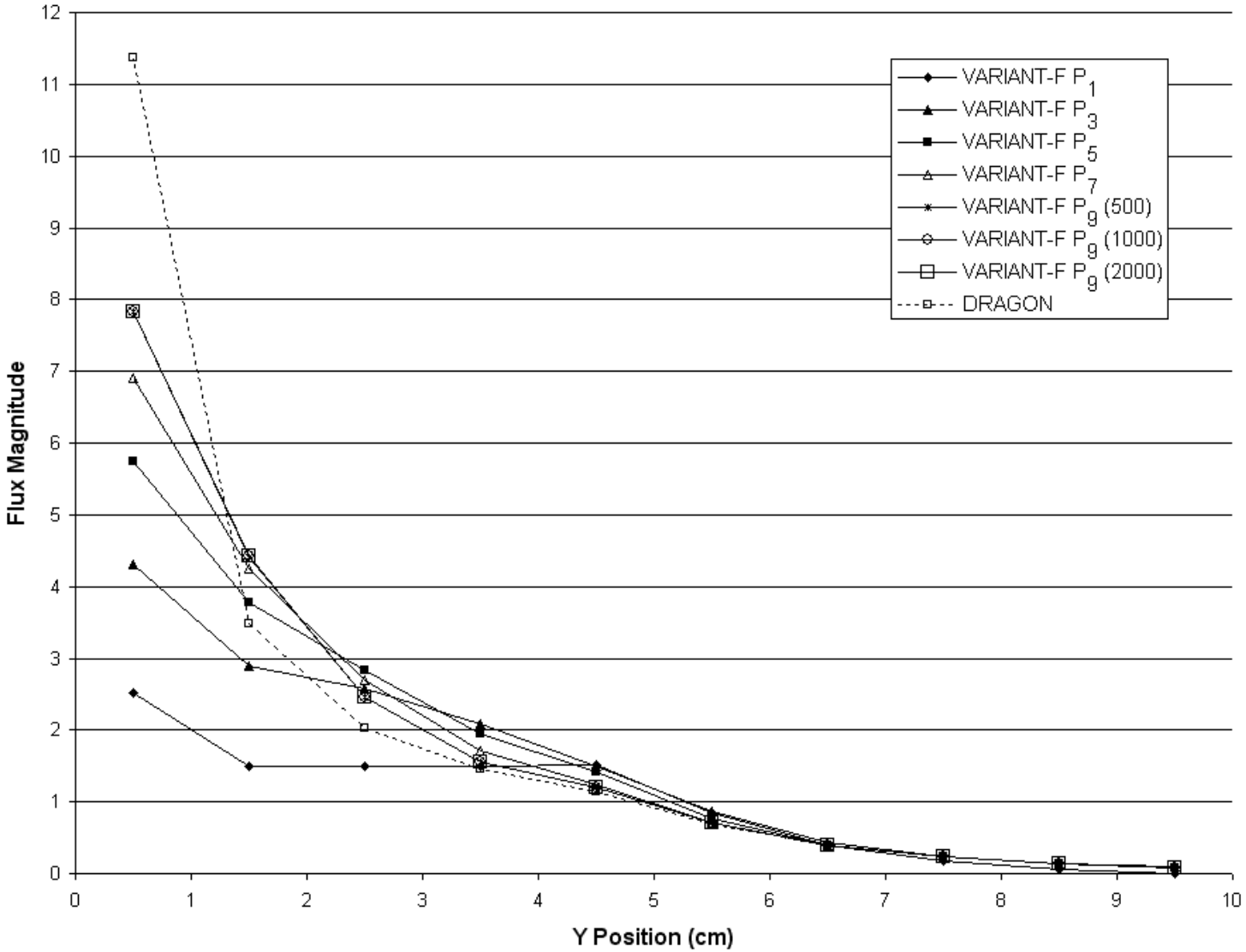

Figure 22. VARIANT-F Solutions to the Watanabe-Maynard Benchmark Problem 2, Diagonal Traverse

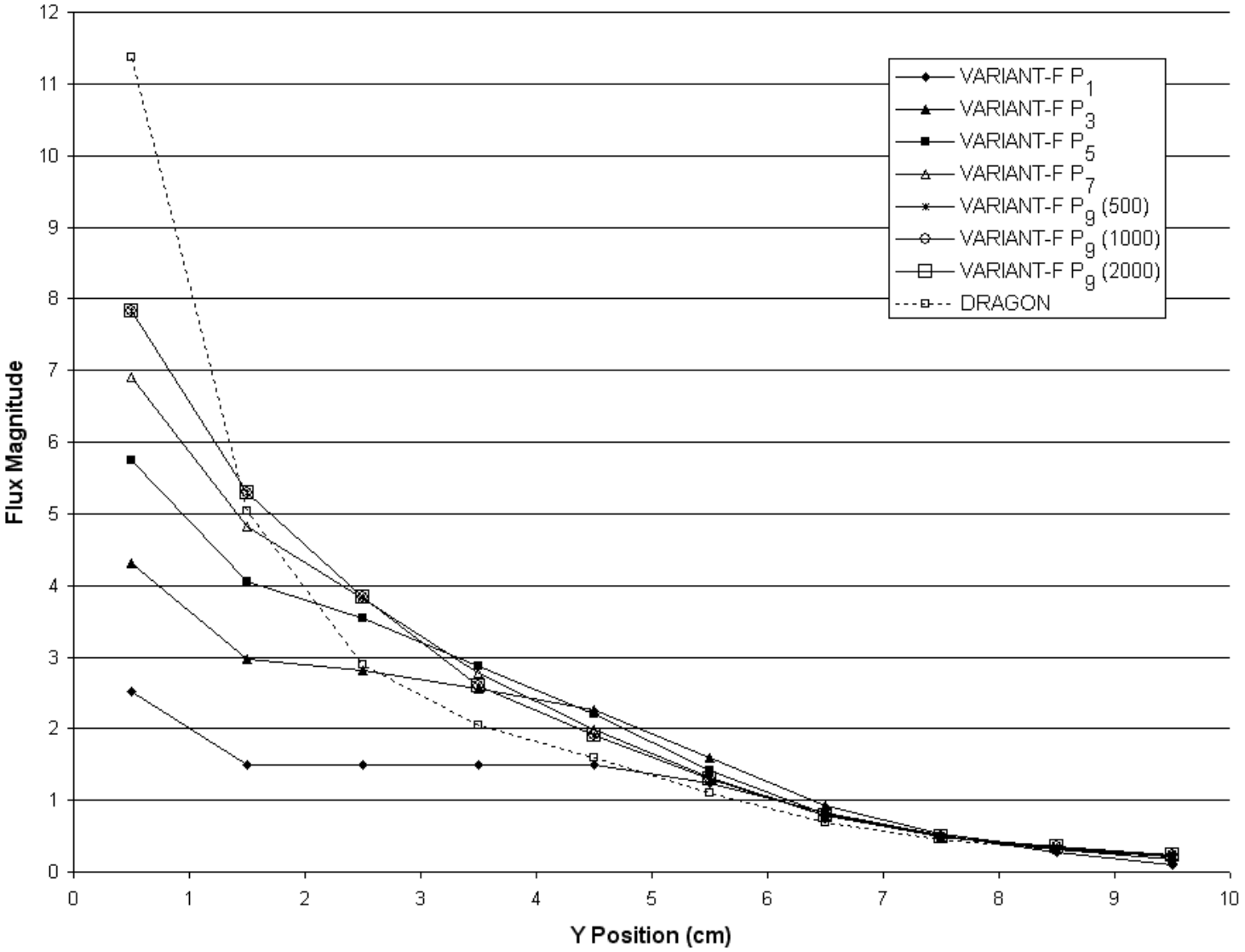

Figure 23. VARIANT-F Solutions to the Watanabe-Maynard Benchmark Problem 2, Reflected Traverse

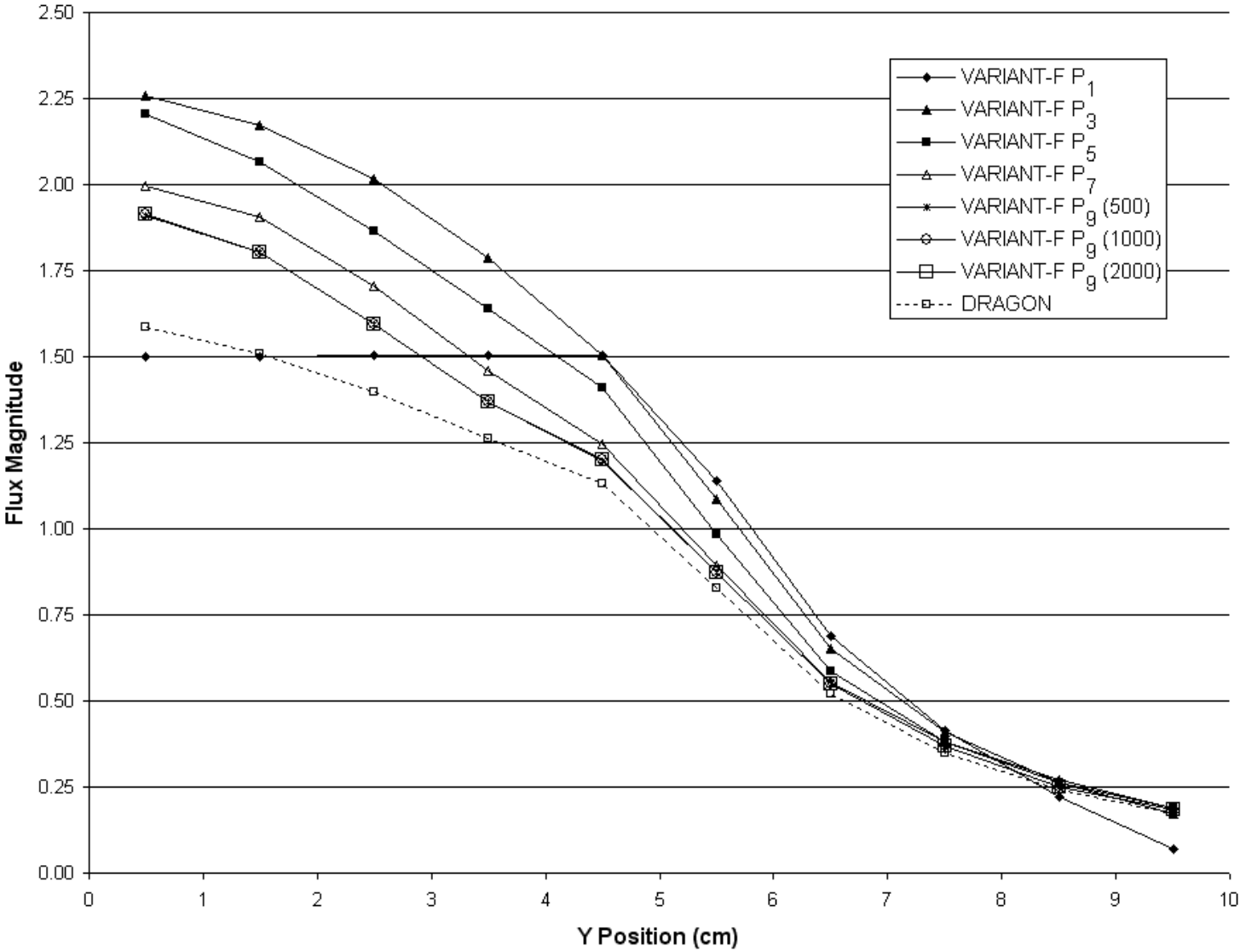

Figure 24. VARIANT-F Solutions to the Watanabe-Maynard Benchmark Problem 2, Void Traverse

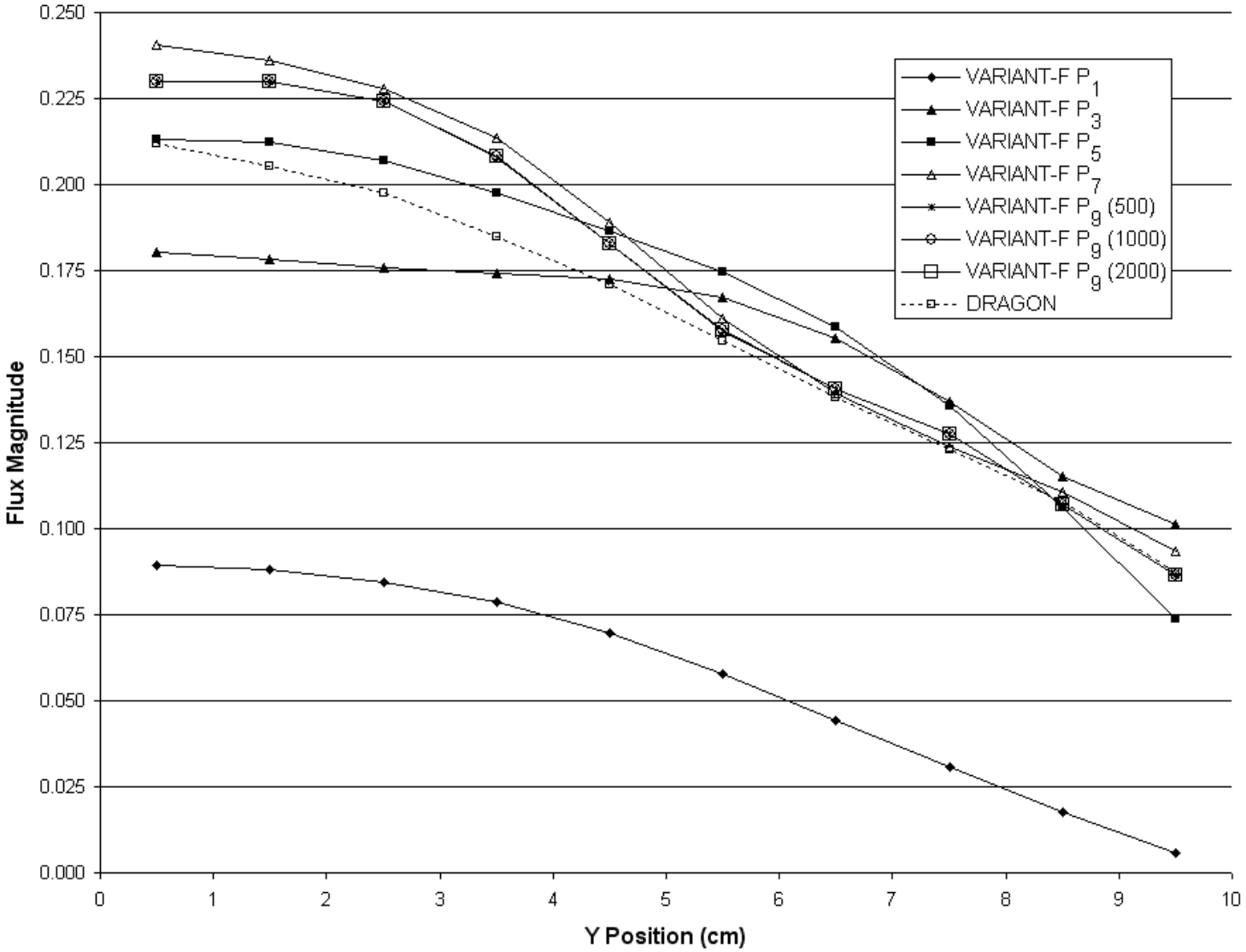

Figure 25. VARIANT-F Solutions to the Watanabe-Maynard Benchmark Problem 2, Vacuum Traverse

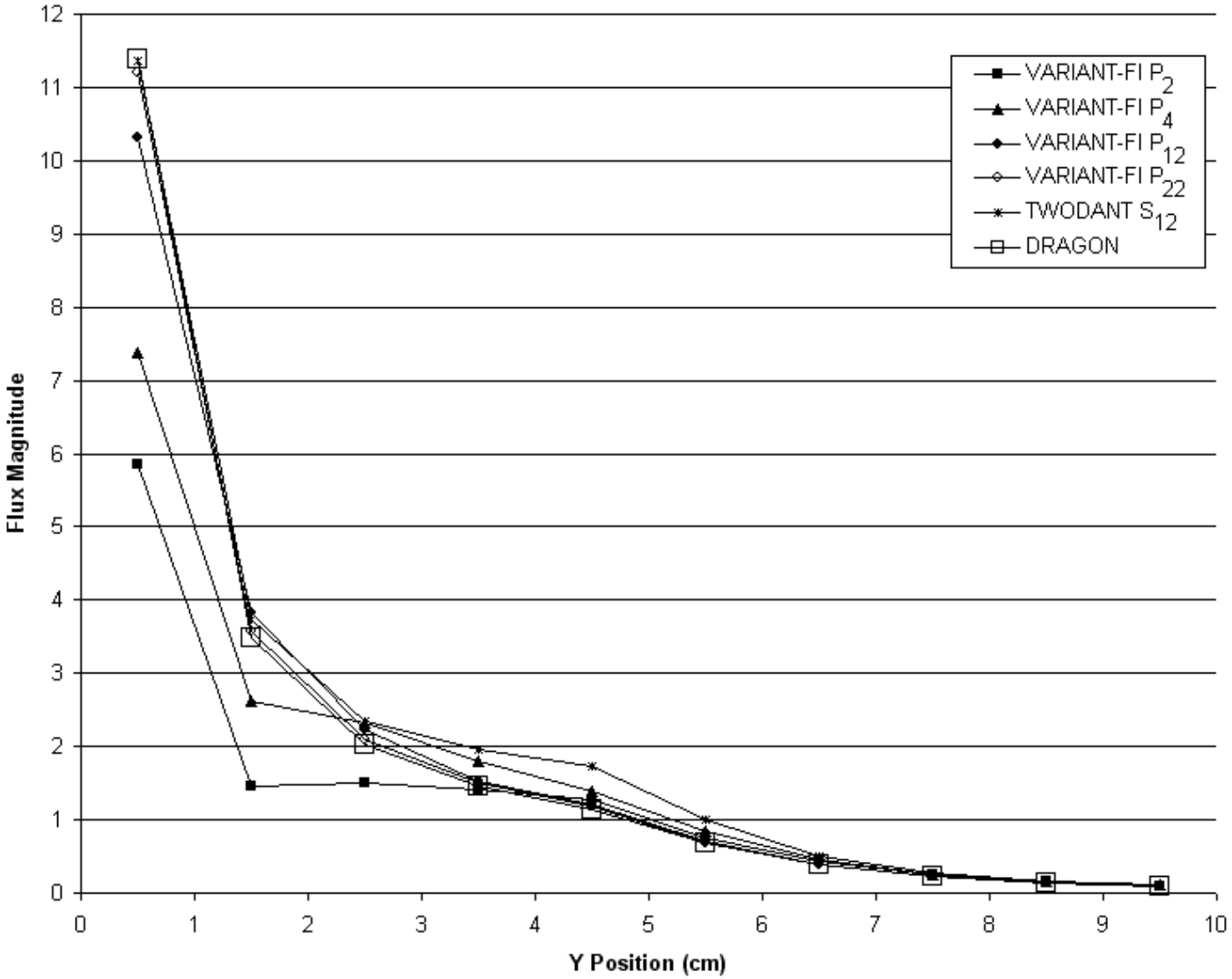

Figure 26. VARIANT-FI Solutions to the Watanabe-Maynard Benchmark Problem 2, Diagonal Traverse

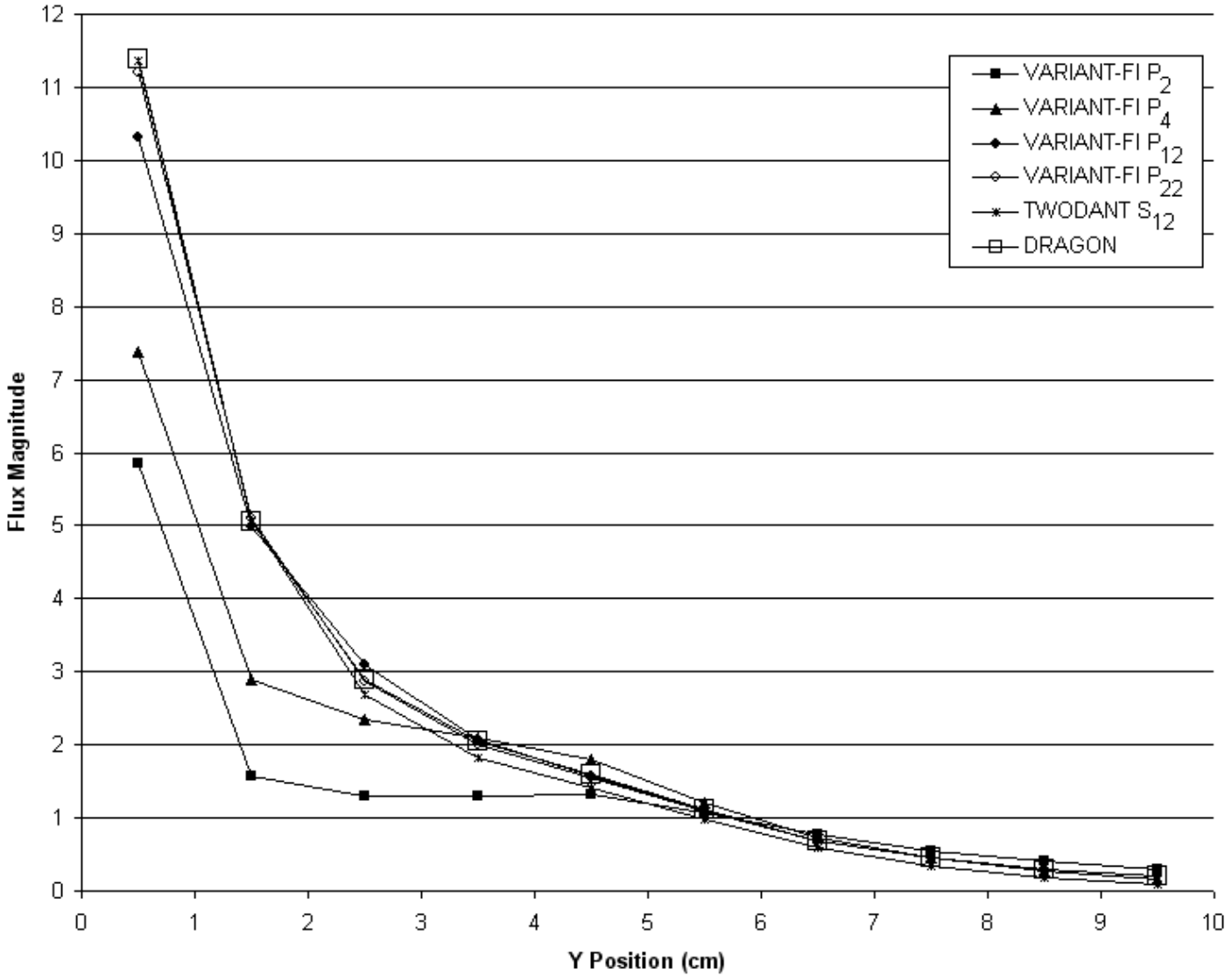

Figure 27. VARIANT-FI Solutions to the Modified Watanabe-Maynard Benchmark Problem 2, Reflected Traverse

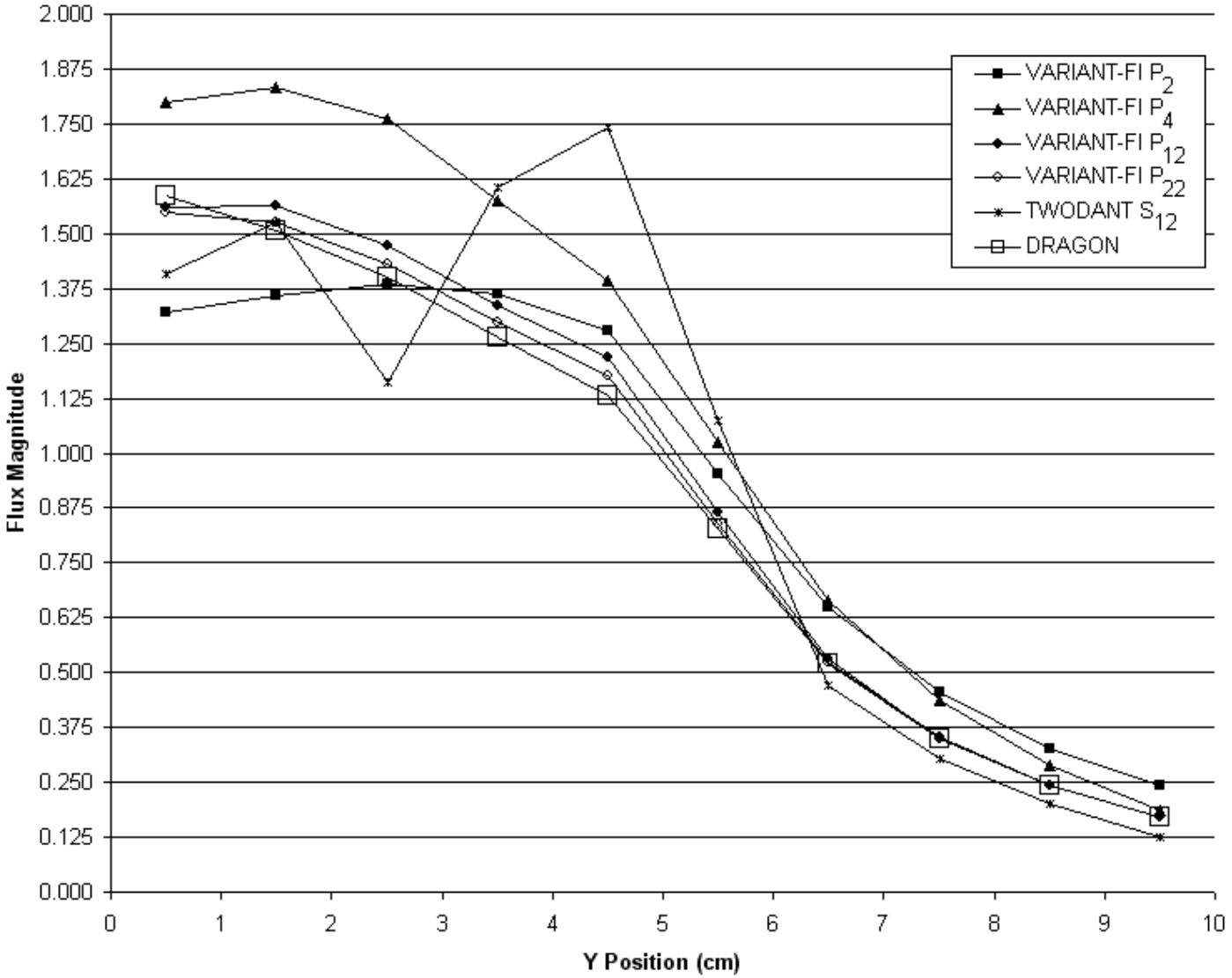

Figure 28. VARIANT-FI Solutions to the Modified Watanabe-Maynard Benchmark Problem 2, Void Traverse

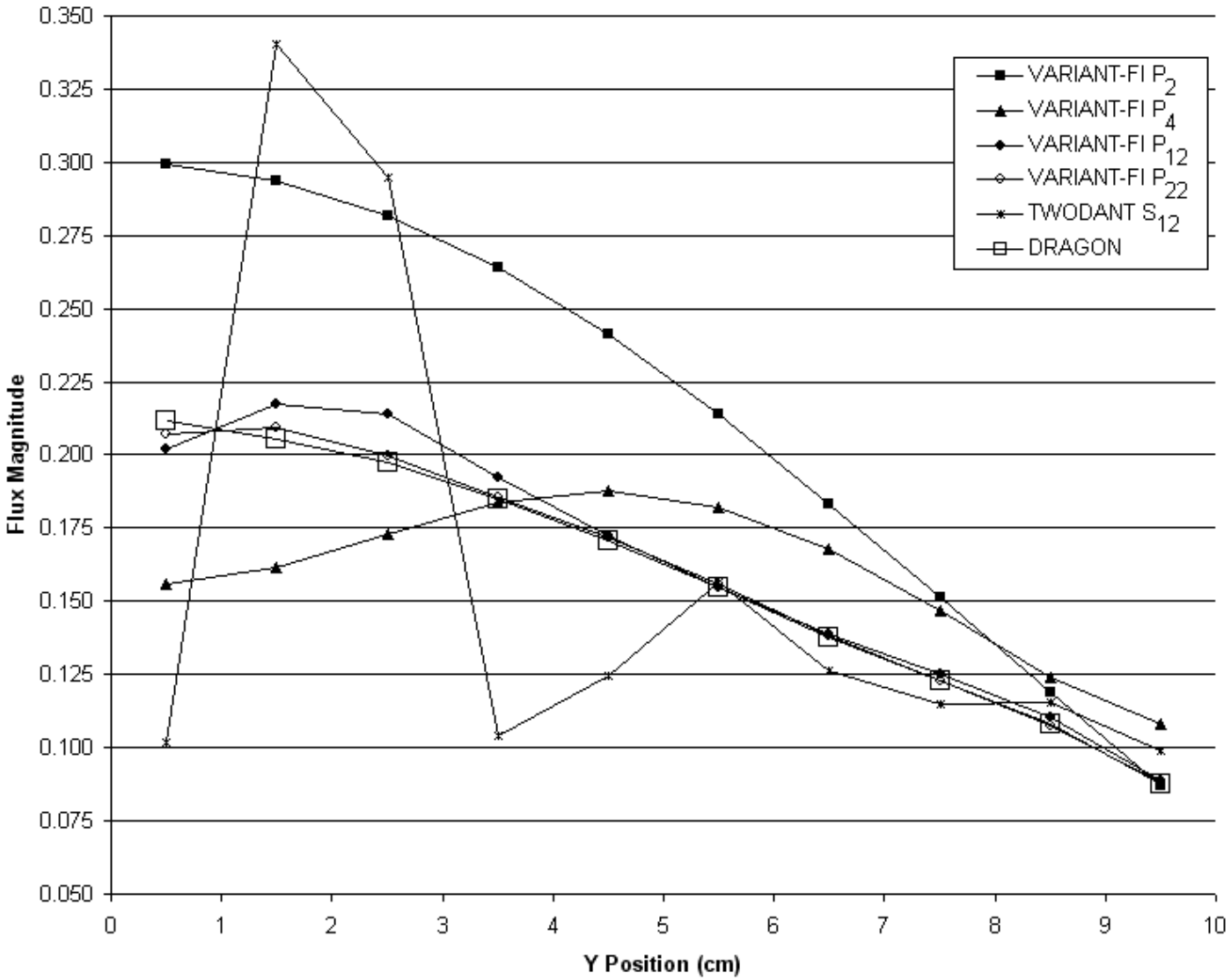

Figure 29. VARIANT-FI Solutions to the Modified Watanabe-Maynard Benchmark Problem 2, Vacuum Traverse

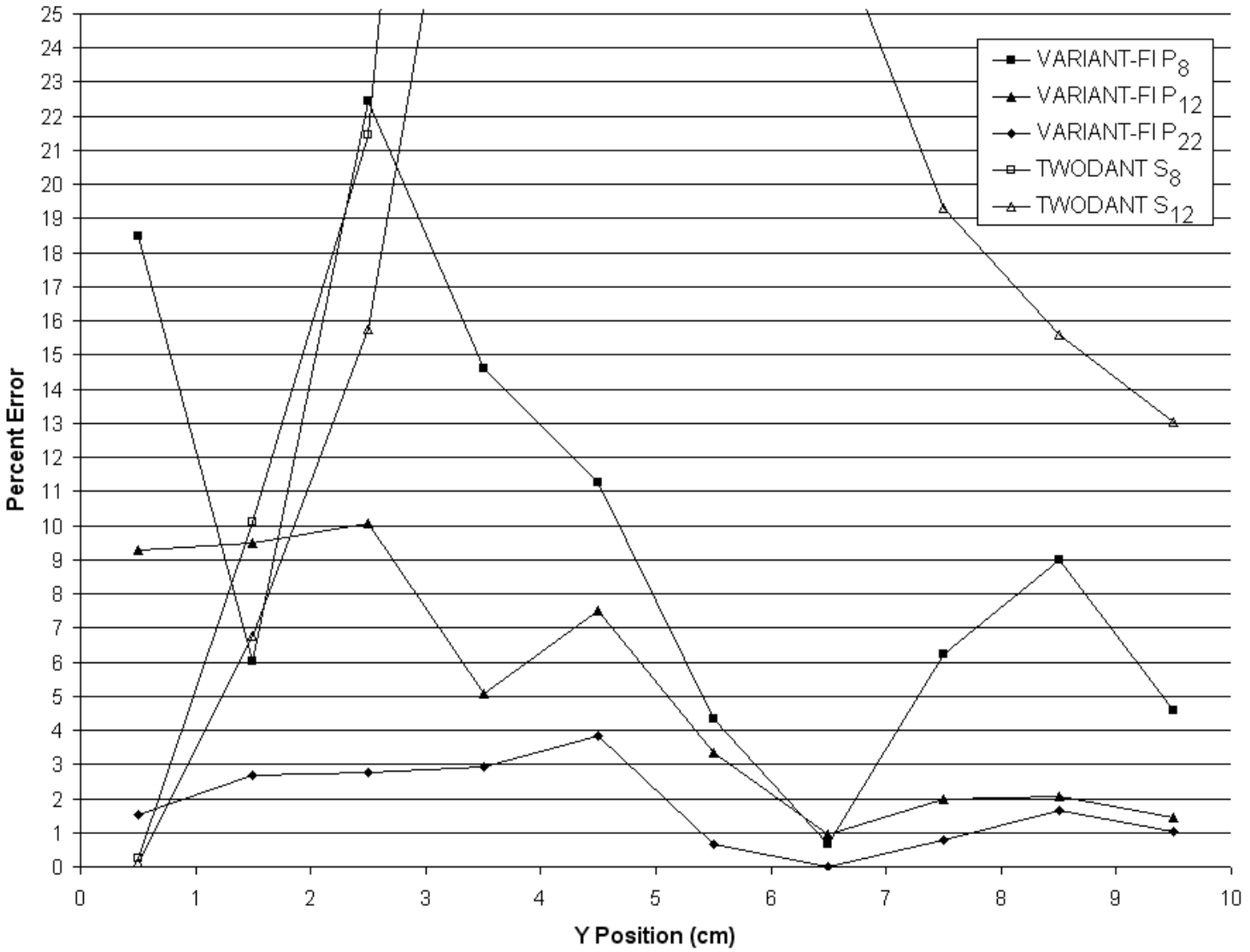

Figure 30. VARIANT-FI and TWODANT Error for the Watanabe-Maynard Benchmark Problem 2, Diagonal Traverse

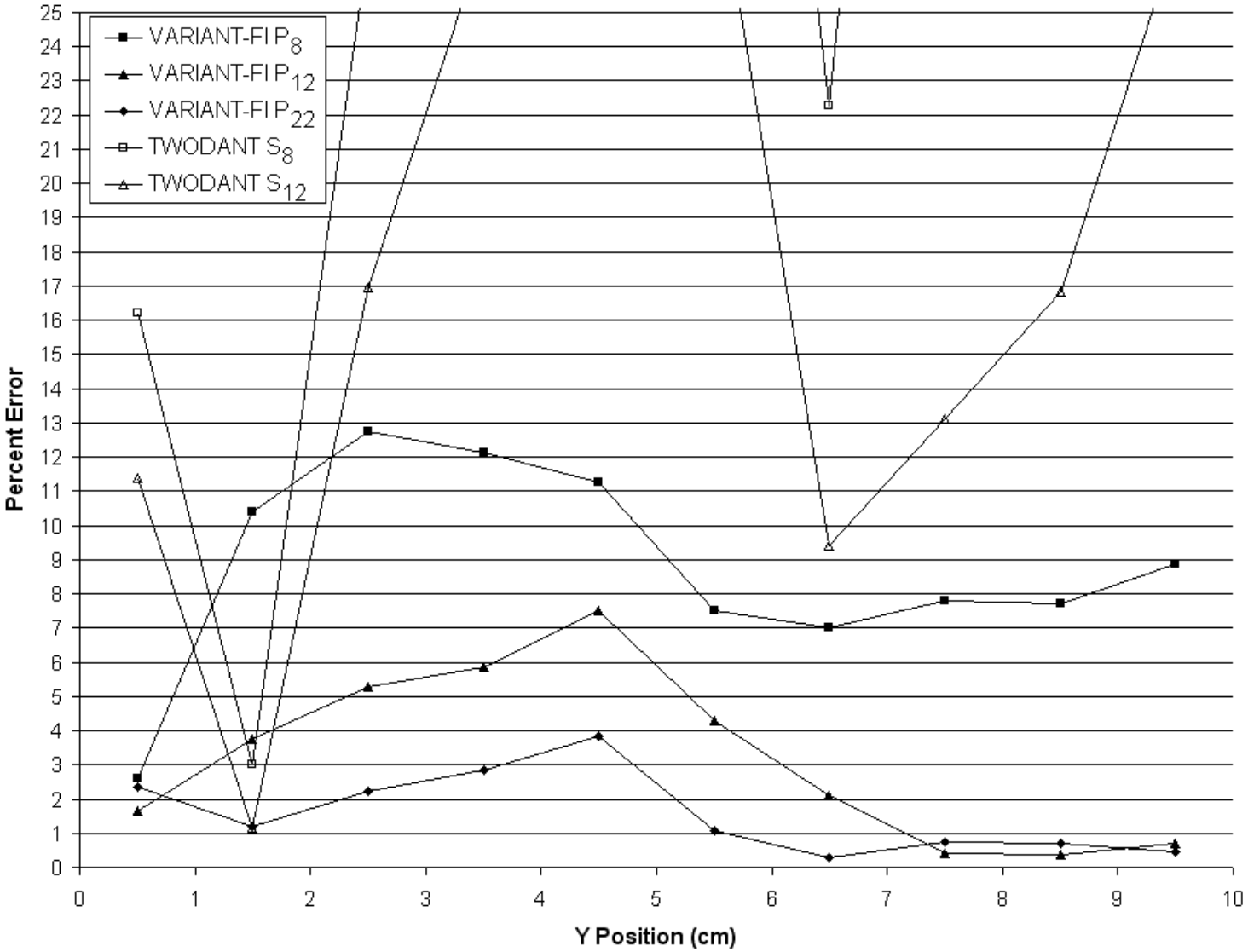

Figure 31. VARIANT-FI and TWODANT Error for the Watanabe-Maynard Benchmark Problem 2, Void Traverse

References

1. C. B. Carrico, E.E. Lewis an dG. Palmiotti, "Three Dimensional Variational Nodal Transport Methods for Cartesian, Triangular and Hexagonal Criticality Calculations," Nucl. Sci. Eng. 111, 168 (1992).
2. G. Palmiotti, E. E. Lewis & C. B. Carrico, "VARIANT: VARIational Anisotropic Nodal Transport for Multidimensional Cartesian and Hexagonal Geometry Calculation," Argonne National Laboratory ANL-95/40, 1995.
3. Mathsoft, Mathcad 6.0 Professional Edition Users Manual. Mathsoft, 1995.
4. G. Palmiotti, C. B. Carrico, and E.E. Lewis, "Variational Nodal Transport Methods with Anisotropic Scattering," Nucl. Sci. Eng. 115, 233-234 (1993).
5. W. S. Yang, M. A. Smith, G. Palmiotti & E. E. Lewis, "Interface Conditions and Angular Trial Functions in Variational Nodal Formulation for Multi-dimensional Spherical Harmonics Method," to be submitted to Nucl. Sci. Eng. (2003).
6. M. A. Smith, G. Palmiotti, E. E. Lewis & N. Tsoulfanidis, "An Integral Form of the Variational Nodal Method," to be published in Nucl. Sci. Eng. (2003).
7. Y. Y. Azmy, "The Weighted Diamond-Difference Form of Nodal Transport Methods," Nucl. Sci. Eng., 98, 29 (1988).
8. G. Marleau, A. Hébert & R. Roy, "A User's Guide for DRAGON," Ecole Polytechnique de Montréal, December 1997.
9. Y. Watanabe and C. W. Maynard, "The discrete cones method in two dimensional neutron transport computations," University of Wisconsin. Report UWFDM-574 (1984).
10. R. E. Alcouffe, F. W. Brinkley, D. R. Marr, and R. D. O'dell, "User's Guide for TWODANT: A Code Package for Two-Dimensional, Diffusion-Accelerated Neutral Particle Transport," LA-10049-M, Los Alamos National Laboratory (1984).
11. W. S. Yang, G. Palmiotti, and E.E. Lewis, "Numerical Optimization of Computing Algorithms of the Variational Nodal Method Based on Transformation of Variables," Nucl. Sci. Eng. 139, 174-185 (2001).